RESEARCH

Open Access

The microenvironment cell index is a novel indicator for the prognosis and therapeutic regimen selection of cancers

Xian-Yan Yang[1,3,4,5†], Nian Chen[1,3,4†], Qian Wen[1,3,4], Yu Zhou[1,3,4], Tao Zhang[1,3,4], Ji Zhou[1,3,4], Cheng-Hui Liang[1,3,4], Li-Ping Han[1,3,4], Xiao-Ya Wang[1,3,4], Qing-Mei Kang[1,3,4], Xiao-Xia Zheng[1,3,4], Xue-Jia Zhai[1,3,4], Hong-Ying Jiang[1,3,4], Tian-Hua Shen[1,3,4], Jin-Wei Xiao[1,3,4], Yu-Xin Zou[1,3,4], Yun Deng[1,3,4], Shuang Lin[2], Jiang-Jie Duan[1,3,4,5], Jun Wang[1,3,4,5*] and Shi-Cang Yu[1,2,3,4,5*]

Abstract

Background It is worthwhile to establish a prognostic prediction model based on microenvironment cells (MCs) infiltration and explore new treatment strategies for triple-negative breast cancer (TNBC).

Methods The xCell algorithm was used to quantify the cellular components of the TNBC microenvironment based on bulk RNA sequencing (bulk RNA-seq) data. The MCs index (MCI) was constructed using the least absolute shrinkage and selection operator Cox (LASSO-Cox) regression analysis. Single-cell RNA sequencing (scRNA-seq), spatially resolved transcriptomics (SRT), and multiplex immunofluorescence (mIF) staining analyses verified MCI. The mechanism of action of the MCI was investigated in tumor-bearing mice.

Results MCI consists of the six types of MCs, which can precisely predict the prognosis of the TNBC patients. scRNA-seq, SRT, and mIF analyses verified the existence and proportions of these cells. Furthermore, combined with the spatial distribution characteristics of the six types of MCs, an MCI-enhanced (MCI-e) model was constructed, which could predict the prognosis of the TNBC patients more accurately. More importantly, inhibition of the insulin signaling pathway activated in the cancer cells of the MCI[high] the TNBC patients significantly prolonged the survival time of tumor-bearing mice.

Conclusions Overall, our results demonstrate that MCs infiltration can be exploited as a novel indicator for the prognosis and therapeutic regimen selection of the TNBC patients.

Keywords Triple-negative breast cancer, Tumor microenvironment, Cell infiltration, Spatial location, Prognosis prediction, Therapeutic regimen

†Xian-Yan Yang and Nian Chen contributed equally to this study.

*Correspondence:
Jun Wang
wangjun@tmmu.edu.cn
Shi-Cang Yu
yushicang@tmmu.edu.cn
Full list of author information is available at the end of the article

Yang *et al. Journal of Translational Medicine* (2025) 23:61

Page 2 of 24

Background

Triple-negative breast cancer (TNBC) is the most aggressive subtype of breast cancer (BC). TNBC is characterized by negative expression of the estrogen receptor (ER), progesterone receptor (PR), and human epidermal growth factor receptor 2 (Her-2) [1]. TNBC has a high incidence of metastasis and distant recurrence, lacks specific targets, and is prone to drug resistance [2], which is closely related to the unique tumor microenvironment (TME), which is different from other subtypes. The TME is a complex environment that tumor cells rely on for survival and development and consists mainly of tumor cells, stromal cells and tissues, the microvasculature, and various chemokines. The presence of the TME enhances the proliferation, invasion, metastasis, and ability of tumor cells to escape the immune system, thus hindering the antitumor response of TNBC [3–5].Treg infiltration in the TNBC microenvironment is significantly greater than that in other BC subtypes, which inhibits an excessive immune response through the secretion of specific cytokines, suggesting that TNBC cells escape the immune system [5, 6]. M1 macrophages in tumor-associated macrophages (TAMs) can kill tumors, whereas M2 macrophages can promote tumor growth and metastasis through the secretion of chemokines or growth factors and are considered important prognostic factors for cancers [4, 7]. TILs are highly infiltrative in TNBC and are associated with prognosis, with $CD4^+$T helper cells and $CD8^+$cytotoxic T cells also playing critical roles in immune defense [3, 7–14]. Similarly, differences in the proportions of non-TILs, such as resting natural killer cells, neutrophils, and macrophages, may be related to differences in cancer prognosis [15].

TME structure may be able to predict cancer subtypes even more accurately than tumor genomic features [16]. However, there has been no systematic investigation into the associations between the overall profile of cell infiltration in the TME and the clinical outcomes of TNBC, lung cancer, and glioblastoma (GBM) patients [17]. Therefore, by analyzing the unique categories and subtypes of the TME, we can comprehensively understand the characteristics of cell infiltration in the TME of cancer patients, improve the ability to predict and control immune responses and uncover new therapeutic targets [18].

In this study, the xCell algorithm was used to evaluate MCs infiltration in the above three cancers based on bulk RNA sequencing (bulk RNA-seq) data and MCI for predicting their prognosis was proposed. The MCI model was subsequently used to verify the feasibility of the prediction model via single-cell RNA sequencing (scRNA-seq), spatially resolved transcriptomics (SRT), and multiplex immunofluorescence (mIF) staining.

Furthermore, MCI was optimized in combination with the spatial distribution characteristics of the six types of MCs, and on this basis, a new TNBC intervention strategy targeting the insulin signaling pathway was tested.

Methods

Data source

The bluk RNA-seq cohorts for TNBC (GSE1456, GSE2603, GSE2990, GSE7390, GSE25055, GSE25065, GSE58812, GSE86166 and GSE53752) and GBM (GSE83300, GSE74187, GSE212067 and GSE13041) were obtained from the Gene Expression Omnibus (GEO) database (http://www.ncbi.nlm.nih.gov/geo/). The other bluk RNA-seq cohorts for TNBC (brca-tcga, brca-tcga-pub2015, and brca-METABRIC) were from the cBio-Portal website (http://www.cbioportal.org/index.do) [19]. The bluk RNA-seq cohorts for lung cancer (called TCGA-LUNG), GBM (called TCGA-GBM), 22 TNBC cell lines, and the immortalized epithelial cell line HMEL (RRID: CVCL_IZ34) in the Cancer Cell Line Encyclopedia (CCLE) database were from UCSC Xena (http://xena.ucsc.edu/). The cell line details were obtained from ExPASy (https://www.ExPASy.org). All bluk RNA-seq cohorts were accessible and included patient overall survival (OS) data [20]. Only the TNBC samples were subjected to subsequent analysis for the TNBC cohorts [21].

The scRNA-seq cohorts for TNBC (GSE118390, GSE75688, GES176078, and GSE161529) were also from the GEO database. GSE118390, GSE75688, and GES176078 contained 6, 5 and 10 TNBC samples, respectively. The SRT cohort for TNBC (called CID4465, CID4497, 1160920F and 114243F) was obtained from the Single-cell Portal database (https://singlecell.broadinstitute.org/single_cell/study/).

Preprocessing of the bluk RNA-seq cohorts

The expression values from various batches or platforms were normalized via the removed batch effect function from the "limma" R package. The bluk RNA-seq cohorts of the eleven the TNBC patients and five GBM patients were combined. To determine if the batch impact was abolished, principal component analysis (PCA) was employed [22].

The eleven bluk RNA-seq cohorts for TNBC were integrated into a combined cohort called *allTNBC* (n = 940) after removing batch effects [23]. Then *allTNBC* was divided into a training cohort called *trainTNBC* (n = 403), and two validation cohorts, called *testTNBC1* (n = 277) and *testTNBC2* (n = 260) were created via 3:2:2 stratified sampling with fivefold cross-validation [24, 25]. The five GBM cohorts were also integrated into a combined cohort (called *allGBM*, n = 377).

Yang *et al. Journal of Translational Medicine*   (2025) 23:61

Page 3 of 24

Estimation of cell infiltration

The xCell algorithm was used to examine the degree of infiltration of 64 immune and stromal cell types. The "xCell" R package (https://github.com/dviraran/xCell) was used to implement the xCell algorithm to determine the proportions of 64 immune cells [26].

Constitution of the MCI

To identify features, LASSO-Cox regression analysis was carried out via the "glmnet" R package [27]. The MCI was calculated based on the relative cell abundance, and the formula was as follows:

$MCI = \sum_{i=1}^{n} (cell_i * Coe_i)$ (where n is the number of signature cells, $cell_i$ indicates the relative abundance of each cell, and Coe_i indicates the corresponding Cox regression coefficient) [27].

Analysis of the TNBC scRNA-seq cohort

Three scRNA-seq cohorts were integrated (called the *allTNBCsc* cohort, n = 21) to perform downstream analysis. The standard protocol of the "Seurat" R package is a very well-established workflow for analyzing scRNA-seq data. The integration step was additionally performed with the "Harmony" R package and used to preprocess the data and reduce batch effects, as these two methods are superior to other integration protocols. Otherwise, the default settings were used for each method. The clustering results were visualized via the t-SNE algorithm.

Analysis of the TNBC SRT cohort

The "Seurat" and "SPATA" R packages were used for basic analysis and visualization. Initially, several standard statistical analyses were carried out for the gene spot matrices. The data were subsequently subjected to basic quality control. Spots with abnormally low nUMI or nGene values were specifically eliminated. The mitochondrial and ribosomal genes were filtered. To find 2000 highly variable genes based on their expression means and variances, the expression matrices were further normalized, log transformed, centered, and scaled. The spots were then projected into a low-dimensional space that was determined by the first 30 main components (PCs) via PCA. Finally, the matrices were subjected to visualization analysis via the TSNE algorithm.

Cosine similarity measurement

Cosine similarity calculates the cosine angle between two cohorts to determine their degree of similarity. Its basic calculation formula is as follows:

$$\cos\theta = \frac{\sum_{i=1}^{n} (A_i \times B_i)}{\sqrt{\sum_{i=1}^{n} (A_i)^2} \times \sqrt{\sum_{i=1}^{n} (B_i)^2}} = \frac{A \cdot B}{|A| \times |B|}$$

Here, A_i and B_i represent the components of cohorts A and B, respectively. The cosine function's output falls between − 1 and 1, meaning that the range of the two cohorts' cosine similarity is [− 1, 1]. The two cohorts coincide and have a similarity of 1 when the angle between them is 0°. The two cohorts are point in opposing directions, and the similarity is − 1 when the included angle is 180°. The cosine similarity was calculated via "numpy" in Python.

Functional enrichment analysis

For the differentially expressed genes (DEGs) between the MCI^{high} and MCI^{low} groups, Kyoto Encyclopedia of Genes and Genomes (KEGG) pathway analysis were performed via the "clusterProfiler" R package. The "limma" R package was used to identify the DEGs identified via bulk RNA-seq and CCLE gene expression data. The "Seurat" R package's FindMarkers function was used to identify the DEGs in the scRNA-seq and SRT cohorts. Only the transcripts with log2FC ≥ ± 1 and $P \leq 0.05$ were considered as DEGs. $P < 0.05$ for KEGG pathways was considered significant [28]. Bayesian network plots for enrichment analysis were created via the "CBNplot" R package [29].

mIF staining [30–32]

Two TNBC tissue microarrays (TMAs) were obtained from Superbiotek ZhuoHao (Shanghai, China) and included 90 TNBC tissue samples and 70 non-TNBC tissue samples (BRC601-1 and BRC601-2). Research has focused mainly on TNBC tissue samples. The clinicopathological parameters included patient age and sex, tumor grade and stage, and survival time and status (Table S9). After filtering out TNBC tissues that were lost during the mIF preparation process and had a total cell count of less than 1000, 65 TNBC tissues remained for analysis. TMA was performed via two antibody panels. Panel 1 (six-marker panel) contained antibodies against CD38 (Abcam, ab108403, EPR4106), CD34 (Abcam, ab81289, EP373Y), CD45RA (Abcam, ab755, 4KB5), CD27 (Abcam, ab131254, EPR8569), and CD19 (Abcam, ab134114, EPR59069). Panel 2 (seven-marker panel) contains antibodies against CD3 (Abcam, ab16669, SP7), IL4 (Abcam, ab239508, C1), CD64 (Abcam, ab140779, OTI3D3), CD11c (CST, 45,581, D3V1E), CD4 (Abcam, ab133616, EPR6855), and CD8 (Abcam, ab101500, SP16). The TMA was heated, dewaxed with xylene, and rehydrated in graded alcohol (5 min of 100% ethanol, 2 times; 5 min of 95% ethanol; 5 min of 90% ethanol; 5 min of 80% ethanol; 5 min of 70% ethanol; 5 min of ddH$_2$O). The TMA slides were then sectioned in a microwave

(45 s at 100% power, 5 min at 20% power) in antigen retrieval buffer (50×concentrated solution (TGCFR5L) diluted with ddH$_2$O). Hydrogen peroxide (3%) was used to remove endogenous peroxidase after the TMA was cooled to room temperature. Following 30 min of blocking with an antibody dilution at room temperature, the primary antibody was added, and the samples were incubated for either 1–4 h at 37 °C or overnight at 4℃. As a secondary antibody, horseradish peroxidase was utilized for 30 min at room temperature. A tyramide signal amplification dye (Opal 7 Color Kit, PerkinElmer, Hopkinton, MA, USA) was applied after the TMAs had been cleaned. For the remaining antibodies, the aforementioned steps were repeated, and before performing another staining cycle, the antibodies were eliminated by microwave treatment (45 s at 100% power, 5 min at 20% power). Afterward, 4′,6-diamidino-2-phenylindole (DAPI) was used to stain each nucleus.

mIF quantitative analysis (phase I)

Images of mIF were captured via the TissueFAXS platform. From the single-color slides, 65 complete TNBC tissue fields were imaged at 20×magnification. For quantitative analysis of the six-marker panel, the entire tissue area was acquired as a digital grayscale image in six channels (CD38-N530, CD34-N570, CD45RA-N620, CD27-N650, CD19-N700, and DAPI). For quantitative analysis of the seven-marker panel, the entire tissue area was acquired as a digital grayscale image in seven channels (CD3-N480, IL4-N520, CD64-N570, CD11c-N620, CD4-N650, CD19-N700, and DAPI). StrataQuest software was used to identify and quantify cells, and cutoff values were calculated in relation to positive controls. To distinguish and identify individual cells in the DAPI image, a nuclear segmentation method was used. Using the effective nucleus, the protein staining signal was identified based on the expression properties of different channel proteins. Depending on the fluorescence intensity and fluorescence area, a threshold value for the division of the positive cells was set. For the six-marker panel, GMPs (CD34$^+$CD38$^+$CD45RA$^+$), MEPs (CD34$^+$CD38$^+$CD45RA$^-$), and memory B cells (CD19$^+$CD27$^+$) were divided and quantified. For the seven-marker panel, γδT (CD3$^+$CD4$^-$CD8$^-$), Th2 cells (CD3$^+$CD4$^+$IL-4$^+$) and cDC (CD11c$^+$CD64$^-$) cells were divided and quantified. The number of the six types of MCs in each tissue site and the total number of cells were counted, and the percentages of the six types of MCs were calculated [33].

HE staining of the bulk tissue microarray

HE staining was performed after mIF imaging. The bulk tissue microarrays were washed twice in xylene for 20 min, in 100%, 95%, 90%, 80%, and 70% ethanol for 5 min, and washed in tap water for 10 min. HE staining was performed for 5 min and the samples were washed in tap water for 1 min. Alcohol fractionation with 1% hydrochloric acid was performed for 30 s (s), the samples were washed with tap water for 1 min, washed with PBS for 30 s to obtain a blue color, and washed with tap water for 1 min. Eosin staining was performed for 2 min, and the sections were washed with tap water for 3 min. To make the sections transparent, alcohol dehydration and xylene treatment were used. Imaging was performed via a digital pathology section scanner (KFBIO, KF-PRO-120) after neutral gum sealing.

mIF quantitative analysis (phase II)

To investigate the spatial distribution characteristics of the six types of MCs in the TNBC tissues, two pathologists combined HE (Fig. 6a) and mIF (Fig. 6b) to outline the special structures in the tumor tissues (Fig. 6c). The meaning of each abbreviation is listed in Table S6. Based on the HE interpretation, the regions of interest (ROIs) were delineated via StrataQuest software, and the results, including the number of cells, distance, and the average area, were calculated and output.

mIF quantitative analysis (phase III)

Image software was used to determine the characteristics of the tissues and cells, including the number of cells (the total number of cells, the number of cells per tertiary lymphoid structure (TLS), and the total number of cells per TLS), the cell ratio (the ratio of the total number of cells of each type to the total number of cells, the ratio of the total number of cells in the TLS to the total number of cells and the ratio of each cell in the TLS to the total number of cells in the TLS), the distance (the average distance between each cell and the TLS and the average distance between each cell and the tumor focus), and the average area and number of TLSs (Table S6).

Constitution of the MCI model based on the topographical characteristics of cells in the TME

Considering the spatial relationships between the six types of MCs and TLSs and tumor tissue, we quantitatively analyzed the distance, infiltration number, density, and other parameters between the six types of MCs and TLSs and tumor tissue in the mIF and retrained the MCI model. First, we included all the quantitative parameters and MCI data and used the LASSO-Cox regression model to select features to construct the MCI-e1 model. Second, the MCI parameters are constructed by the ratio of the six types of MCs,which have a strong correlation. When constructing a model, only one parameter needs to be accounted for. Therefore, after removing the MCI

Yang *et al. Journal of Translational Medicine*   (2025) 23:61

Page 5 of 24

parameters, we constructed the MCI-e2 model via the remaining parameters. Similarly, we retained the MCI, removed the ratio of the six types of MCs, and constructed the MCI-e3 model. The formula of the MCI-e was as follows:

MCI - e $= \sum_{i=1}^{n}$ (feature$_i$* Coe$_i$)(where n is the number of features, feature$_i$ indicates the MCI and quantitative spatial features in the *mIF* cohort of each cell, and Coe$_i$ indicates the corresponding Cox regression coefficient).

Survival analyses

The individuals were divided into high and low groups according to the best cutoff value according to the surv_ cutpoint function of the "survminer" R package. The "survival" R package was used for KM analysis. The time-dependent ROC curve was used to evaluate the model via the "pROC" R package. Log-rank *P* values, hazard ratios (HRs), and 95% confidence intervals (CIs) were examined [34].

Animal model and dosage regimen

HNMPA was purchased from Target MOI (Shanghai, China, lot #159,969) and dissolved in 5% Tween-80 and 95% ddH$_2$O; DOX was obtained from Shenzhen Main Luck Pharmaceuticals, Inc. (China, 2204E3). All the mice were maintained in a temperature-controlled and pathogen-free environment with 12-h light/dark cycles and food and water ad libitum. Fifty-six 8-week-old female NOD-SCID mice were obtained from Ensweier Biotechnology Co., Ltd. (China). The mice in the different groups (NC=13, DOX=13, HNMPA=15, Combination=15) were treated with the corresponding solutions twice a week for 1 week, and the mice were subjected to intragastric administration and tail vein injection of saline or DOX once a month (Table S8, Fig. 8a). Tumor size was measured and recorded five days after the first treatment. The animals were sacrificed when they reached the endpoint or signs in accordance with the EU Directive 63/2010 and our Ethics Committee advice. Animal tissue samples were fixed with 4% paraformaldehyde (PFA) for >48 hours, embedded in paraffin, embedded in paraffin and cut into 5 μm thick sections. The sections in immunohistochemical were incubated with anti-Ki67 (CST,lot 12202, 1:100) antibodies and stained via an Envision

System (Dako, K3468). Whole-slide images were captured via a KF-PRO-120 digital slide scanner (KFBIO, Ningbo, China). IF staining sections were incubated with p-AKT, (BIOSS, BS-0876R, 1:100) p-ERK (BIOSS, BS-2637R, 1:100), or anti-CD45 (Biolegend, 109837, 1:100) antibodies and were captured via Zessis. Image-Pro Plus V.6.0 software was used for quantitative analysis.

Statistical analysis

Statistical analysis was performed via R, Python, and GraphPad Prism software version 8.0. Data consistency was checked via cosine similarity. The Student's t test (two-tailed) and Mann–Whitney U test were used to determine the significance of the difference between two groups of data. KM analysis was performed via the log-rank test. Contingency table analysis was performed via the χ^2 test. Univariate and multivariate survival analyses of variance for prognostic predictors were performed via Cox proportional hazards models, and comparisons were performed via the Mantel-Cox log-rank test. *P* < 0.05 was considered to indicate statistical significance.

Results

Using bulk RNA-seq data to construct prognostic models based on MCs infiltration

We used the removeBatchEffect method to eliminate the batch effects in the eleven TNBC cohorts. Pre- (Figure S1a) and post-standardized (Figure S1b) data clearly revealed that the batch effect that arose on different platforms was eliminated (Figure S1a, b).

Next, we used the xCell algorithm to calculate the cell fraction in the TNBC bulk RNA-seq cohorts (*allTNBC, trainTNBC, testTNBC1,* and *testTNBC2*) and revealed that the TNBC enriches immature dendritic cells, hematopoietic stem cells (HSCs), mesenchymal stem cells (MSCs), and common lymphoid progenitor cells (CLPs), etc. (Fig. 1a). The relative abundances of the 64 types of MCs in the *trainTNBC, testTNBC1,* and *testTNBC2* cohorts were highly consistent (Figure S2a-c). MCs were subsequently applied to the LASSO-Cox regression model to construct a predictive model called MCI for OS in the train*TNBC* cohort. The six types of MCs, including granulocyte–macrophage progenitor cells (GMPs), megakaryocyte-erythroid progenitor cells (MEPs), memory B

(See figure on next page.)

Fig. 1 Distribution, feature selection, and data consistency analysis of TME-infiltrating cells in TNBC. **a** Percentages of 64 types of MCs in the *allTNBC* cohort (n=940). **b** LASSO-Cox regression model for feature selection via tenfold cross-validation in the *trainTNBC* cohort. **c**, Plots for LASSO-Cox regression coefficients over different values of the penalty parameter. **d**–**g** Percentages of the six types of MCs associated with MCI in the *allTNBC* (**d**), *trainTNBC* (n=403) (**e**), *testTNBC*1 (n=277), (**f**) and *testTNBC*2 (n=260) (**g**) cohorts. **h**–**j** The cosine similarity algorithm was used to analyze the consistency of the proportions of the six types of MCs associated with MCI in *trainTNBC* (**h**), *testTNBC*1 (**i**), *testTNBC*2 (**j**), and *allTNBC*. The heights of the bar charts represent different proportions. The higher the ratio is, the stronger the consistency of the data
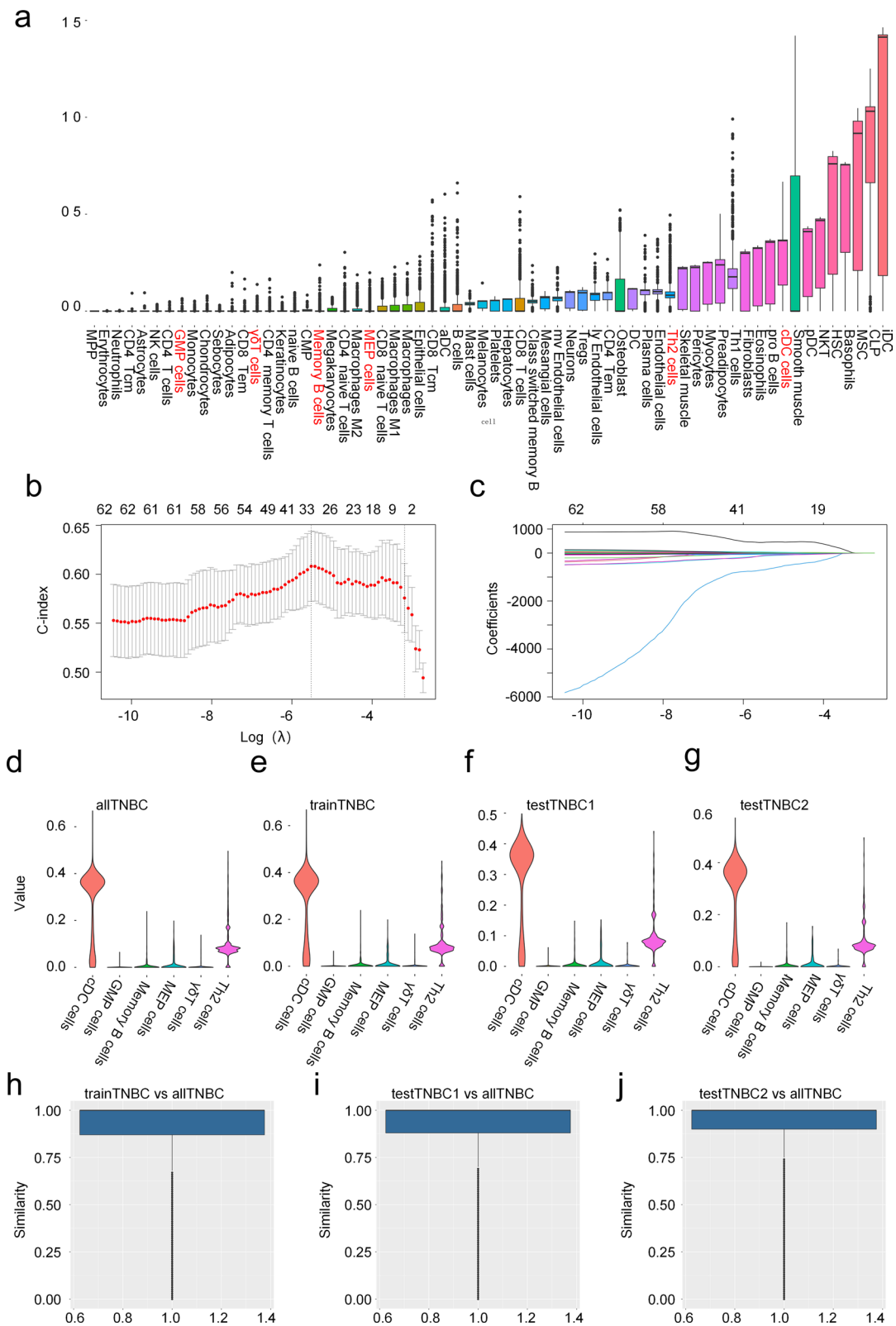
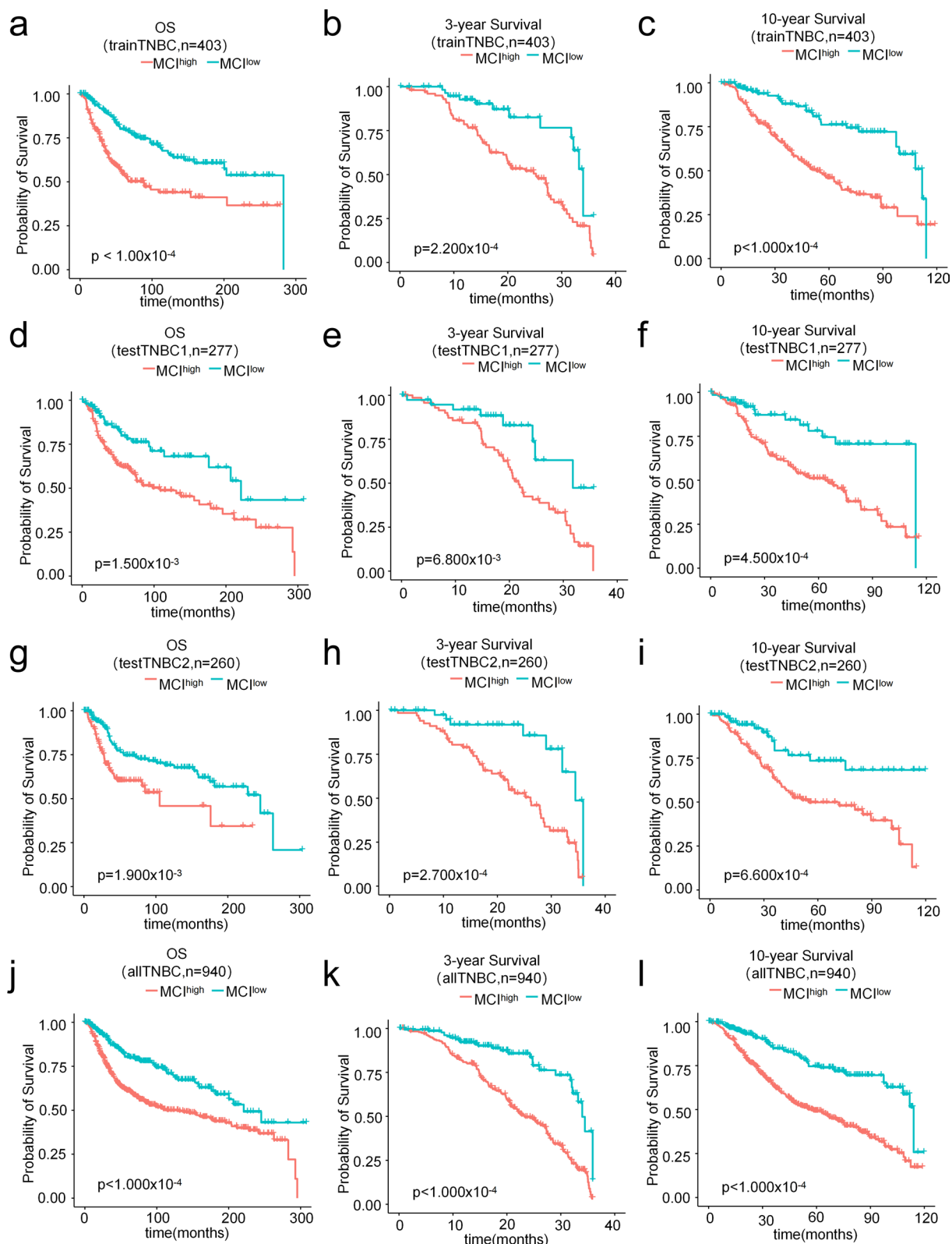**Fig. 1** (See legend on previous page.)

Fig. 2 Prediction of the prognosis of the TNBC patients by MCI. **a-l**, KM analysis of OS (**a**, **d**, **g**, **j**), 3-year survival (**b**, **e**, **h**, **k**) and 10-year survival (**c**, **f**, **i**, **l**) between the MCI groups in the *trainTNBC* (**a–c**), *testTNBC*1 (**d–f**), *testTNBC*2 (**g–i**), and *allTNBC* (**j–l**) cohort

Yang *et al. Journal of Translational Medicine*   (2025) 23:61

Page 8 of 24

cells, gamma delta T (γδT) cells, type 2 T helper (Th2) cells and conventional dendritic cells (cDCs), were selected according to the partial likelihood deviance method, and the corresponding coefficients were generated at the optimal log λ of −3.19 (Fig. 1b, c). The relative abundances of these six types of MCs in the *allTNBC*, *trainTNBC*, *testTNBC1,* and *testTNBC2* cohorts are shown in Fig. 1d–g. According to the results of the cosine similarity algorithm evaluation, the relative abundances of the six types of MCs in the *trainTNBC*, *testTNBC1*, and *testTNBC2* cohorts were highly similar to those in the *allTNBC* cohort (Fig. 1h–j). In addition, the MCI of each sample was generated (Table S1) with the formula $MCI = GMPs \times (−7.259) + MEPs \times 2.383 + memory\ B\ cells \times (−3.185) + γδT\ cells \times (−1.626) + Th2\ cells \times 0.879 + cDCs \times (−0.175)$. KM analysis revealed that the MCI was significantly correlated with the OS ($P < 1.000 \times 10^{-4}$, Fig. 2a), 3-year survival probability ($P = 2.200 \times 10^{-4}$, Fig. 2b), and 10-year survival probability ($P < 1.000 \times 10^{-4}$, Fig. 2c) of the TNBC patients in the *trainTNBC* cohort. The TNBC patients with an MCI[high] status had a poor prognosis. The area under the curve (AUCs) of the OS, 3-year survival, and 10-year survival were 0.618, 0.653, and 0.612, respectively (Figure S1c), indicating that the MCI had high accuracy.

We used the *testTNBC1*, *testTNBC*2, and *allTNBC* cohorts for validation. The MCI performed well in these cohorts, which were divided into two groups, MCI[high] and MCI[low], with significant differences in prognosis and OS (Fig. 2d, g, j), and the 3-year survival probability (Fig. 2e, h, k), and 10-year survival probability (Fig. 2f, i, l) of the TNBC patients with MCI[high] were significantly shorter. The AUCs of the OS, 3-year survival, and 10-year survival also indicated that MCI had high accuracy (Figure S1d-f). In addition, the AUCs for the MCI and the six types of MCs alone in the TNBC patients were 0.665 (MCI), 0.595 (Th2 cells), 0.407 (cDCs), 0.552 (MEPs), 0.490 (GMPs), 0.479 (γδT cells), and 0.480 (memory B cells) (Figure S1g). The MCI was more accurate in predicting the prognosis of the TNBC patients than the six types of MCs alone.

In the *allTNBC*, *trainTNBC*, *testTNBC1,* and *testTNBC2* cohorts, contingency table analysis revealed that MCI[high] status was associated with high T stage, high N stage, and high AJCC stage in the TNBC patients (Table S2). Univariate regression analysis revealed that MCI[high] was a risk factor for short OS in the TNBC patients (Table S3). Cox multivariate regression analysis revealed that MCI[high] was an independent predictor of short OS in the TNBC patients (Table S3).

Next, we compared MCI-based TNBC typing (MCI[high] and MCI[low]) with TNBC molecular typing, including two basal-like (BL1 and BL2), an immunomodulatory (IM), a mesenchymal (M), a mesenchymal stem-like (MSL), and a luminal androgen receptor (LAR) subtype, introduced by Lehmann/Pietenpol et al. [35]. The results revealed that our two subtypes included all the subtypes of Lehmann's classification and that patients with the IM subtype were mainly distributed in the MCI[low] subtype (Figure S1h). Immune response-related genes are highly expressed in the IM subtype. In addition, Burstein et al. [36] performed a cluster analysis of the mRNA expression profiles of 198 TNBC samples and identified four different TNBC subtypes [36], including LAR, mesenchymal (MES), basal-like immunosuppressed (BLIS), and basal-like immune-activated (BLIA). Among them, BLIA has the best prognosis and BLIS has the worst prognosis. We compared the MCI typing system with those described by Burstein et al. for TNBC molecular subtypes [36]. The MCI subtype included all the subtypes of Burstein et al., and the BLIA subtype was mainly distributed in the MCI[low] subtype (Figure S1i).

To evaluate whether this strategy for constructing MCI in the TNBC patients is applicable to other cancers, we explored the specificity of the MCI in non-TNBC, GBM, and lung patients.we analyzed the expression of the MCI in the GSE86166 dataset, which included non-TNBC patients, and found that MCI was significantly increased in the TNBC patients and that MCI was not statistically significant in predicting the prognosis of the non-TNBC patients (Figure S3a, b). Similarly, The MCI cannot be used to evaluate the prognosis of GBM patients in the TCGA-GBM dataset (Figure S3c). Although it has statistical significance for the prognosis of lung cancer patients, it is slightly less significant compared to MCI[LUNG], which was constructed from the lung cancer microenvironment itself in the TCGA-LUNG dataset (Figure S3d, g).

(See figure on next page.)
Fig. 3 Analysis of the distributions of the six types of MCs associated with MCI in the TNBC tissues using the *allTNBCsc* and SRT cohorts. **a** t-SNE maps of the six types of MCs in the *allTNBCsc* cohort. **b** Percentages of the six types of MCs associated with MCI in the *allTNBCsc* cohort. **c** Consistency of the proportions of the six types of MCs associated with MCI in the *allTNBCsc*, *allTNBC*, and *trainTNBC* cohorts. **d–g** Distributions of the six types of MCs associated with MCI in the SRT cohorts 114243f (**d**), 1160920f (**e**), CID4465 (**f**), and CID44971 (**g**). **h** Percentages of the six types of MCs associated with MCI in the *allTNBCSRT* cohort. **i** The consistency of the proportions of the six types of MCs associated with MCI in the *allTNBCSRT*, *trainTNBC*, and *allTNBC* cohorts
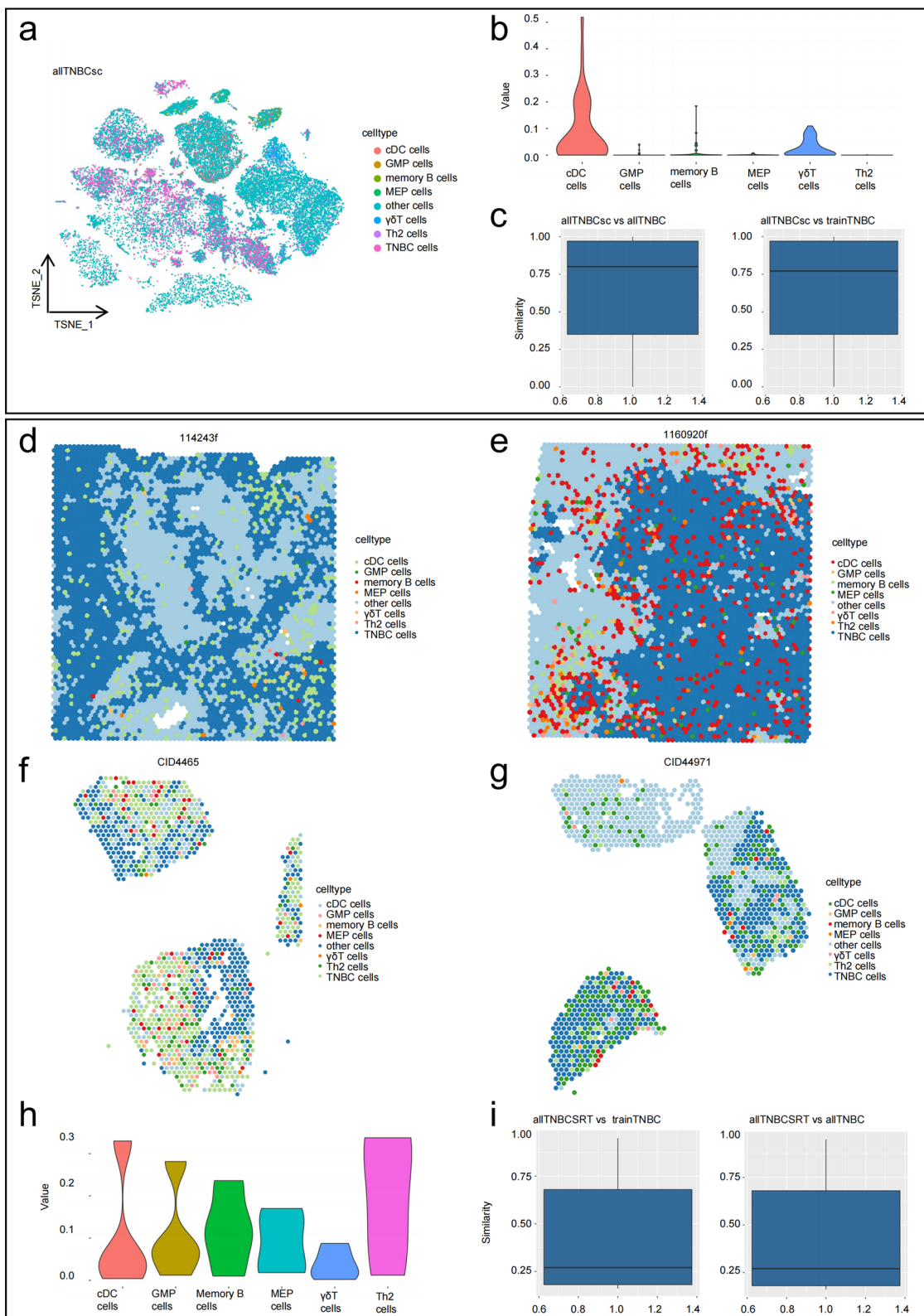
Fig. 3 (See legend on previous page.)

we then use the MCs of the lung and GBM to train their MCI in published lung cancer (TCGA-LUNG, n=820) and combined GBM bulk RNA-seq cohorts (called *allGBM*, n=377). The MCI of each sample was generated with the following formula: (1) $MCI^{LUNG} = CD4^+Tcm \times (-5.675) + Class\text{-}switched\ memory\ B\ cells \times (-3.663) + Eosinophils \times (-6.475) + Mesangial\ cells \times (8.266) + Th2\ cells \times (0.528)$ (Figure S3e). (2) $MCI^{GBM} = Class\text{-}switched\ memory\ B\ cells \times (-2.521) + HSC \times (-0.056) + Macrophages\ M1 \times (0.089) + Mast\ cells \times (-0.193) + Preadipocytes \times (-0.560)$ (Figure S3f). KM analysis revealed that MCI^{LUNG} and MCI^{GBM} were significantly correlated with OS in the TCGA-LUNG ($P < 1 \times 10^{-4}$, Figure S3g) and *allGBM* ($P = 3.100 \times 10^{-4}$, Figure S3h) cohorts and that patients with MCI^{high} had a poor prognosis. The AUCs were 0.596 in both the TCGA-LUNG cohort and the *allGBM* cohort (Figure S3i, j). This finding indicated a favorable predictive value of the MCI. The above results revealed that the MCI has significant value in predicting the prognosis of the patients with TNBC and other solid tumors.

scRNA-seq, SRT, and mIF staining data verified the MCs infiltration profile

We next sought to determine whether the six types of MCs associated with MCI actually exist in the TNBC tumor tissues.

We used the "Harmony" R package to integrate of three TNBC scRNA-seq cohorts (called *allTNBCsc*), and similar clusters of the six types of MCs were identified by the expression of marker genes determined in previous studies (Fig. 3a). t-Distributed stochastic neighbor embedding (tSNE) revealed that the six types of MCs associated with MCI actually existed in the TNBC tissues (Fig. 3a, b). Cosine similarity algorithm analysis revealed that the proportion distributions of the six types of MCs in the *allTNBCsc* cohort were highly similar to those in the *allTNBC* and *trainTNBC* cohorts (Fig. 3c). In addition, we used the scRNA-seq dataset GSE161529, which contains data from non-TNBC patients, to validate MCI and found that there were differences in the six types of MC cells and MCI between the TNBC and non-TNBC patients, especially those that were significantly enriched in the TNBC patients (Figure S4a, b).

To further verify the existence and quantitative proportions of the six types of MCs associated with MCI in the TNBC tumor tissues, we analyzed the TNBC SRT cohort (CID44971, 114243F, CID4465, and 1160920F) published by Wu, S.Z. et al. [37]. By combining the determination of tumor tissue boundaries by pathologists (Figure S4c, f, i, l) and the marker genes of the six types of MCs (Figure S4d, g, j, m), different cell subsets in the TNBC tissue sections were identified (Fig. 3d–g, Figure S4e, h, k, n). The results revealed that the above six types of MCss of the MCI existed in the TNBC tissues (Fig. 3h). the six types of MCs in four SRT samples infiltrated the core area of the tumor to different extents (Fig. 3d–g). Specifically, the six types of MCs infiltrated the tumor tissue, especially γδT cells, Th2 cells, and memory B cells, and were distributed around the tumor cells in the CID4465 sample. The distance between the cells was very small, indicating that there might be an interaction between them and the tumor cells (Fig. 3e).

We combined the cell counts from four SRT cohorts to form the combined SRT cohort (called *allTNBCSRT*). Similarly, cosine similarity algorithm analysis indicated that the number and proportion distributions of these cells in the *allTNBCSRT* cohort were similar to those in the *allTNBC* and *trainTNBC* cohorts (Fig. 3i).

However, regardless of whether bulk RNA-seq, scRNA-seq, or SRT was used, the above results were based on mRNA expression levels. Evidence at the protein expression level was needed further confirm the existence and quantitative proportions of the above six types of MCs of the MCI in the TNBC tumor tissues. Therefore, mIF staining was used to label the tissue microarray of the TNBC patients (called *mIF* cohort, n=65) and annotate the six types of MCs with related markers (Fig. 4a). The results revealed that the above six types of MCs of the MCI existed in the TNBC tissues (Fig. 4b). Similarly, cosine similarity algorithm analysis revealed that the numbers and proportion distributions of these the six types of MCs in the *mIF* cohort were similar to those in the *allTNBC* and *trainTNBC* cohorts (Fig. 4c). More importantly, each patient's MCI was generated via the relative abundance of MC from protein expression data,

(See figure on next page.)

Fig. 4 Quantity, data consistency analysis, and prognostic significance of the six types of MCs in the TNBC tissues array samples. **a** The six types of MCs associated with MCI in the TNBC tissues in the *mIF* cohort (n=65). GMPs, $CD34^+CD38^+CD45RA^+$; MEPs, $CD34^+CD38^+CD45RA^-$; memory B cells, $CD19^+CD27^+$; γδT cells, $CD3^+CD4^-CD8^-$; Th2 cells, $CD3^+CD4^+IL\text{-}4^+$; and cDCs, $CD11c^+CD64^-$. Representative images of nuclei stained with DAPI (blue) are shown. Scale bar=5 μm. **b** Percentages of the six types of MCs associated with MCI in the *mIF* cohort. **c** The consistency of the proportions of the six types of MCs associated with MCI in the *allTNBC*, *trainTNBC,* and *mIF* cohorts. **d** OS comparison between patients with MCI^{high} and MCI^{low} in the *mIF* cohort
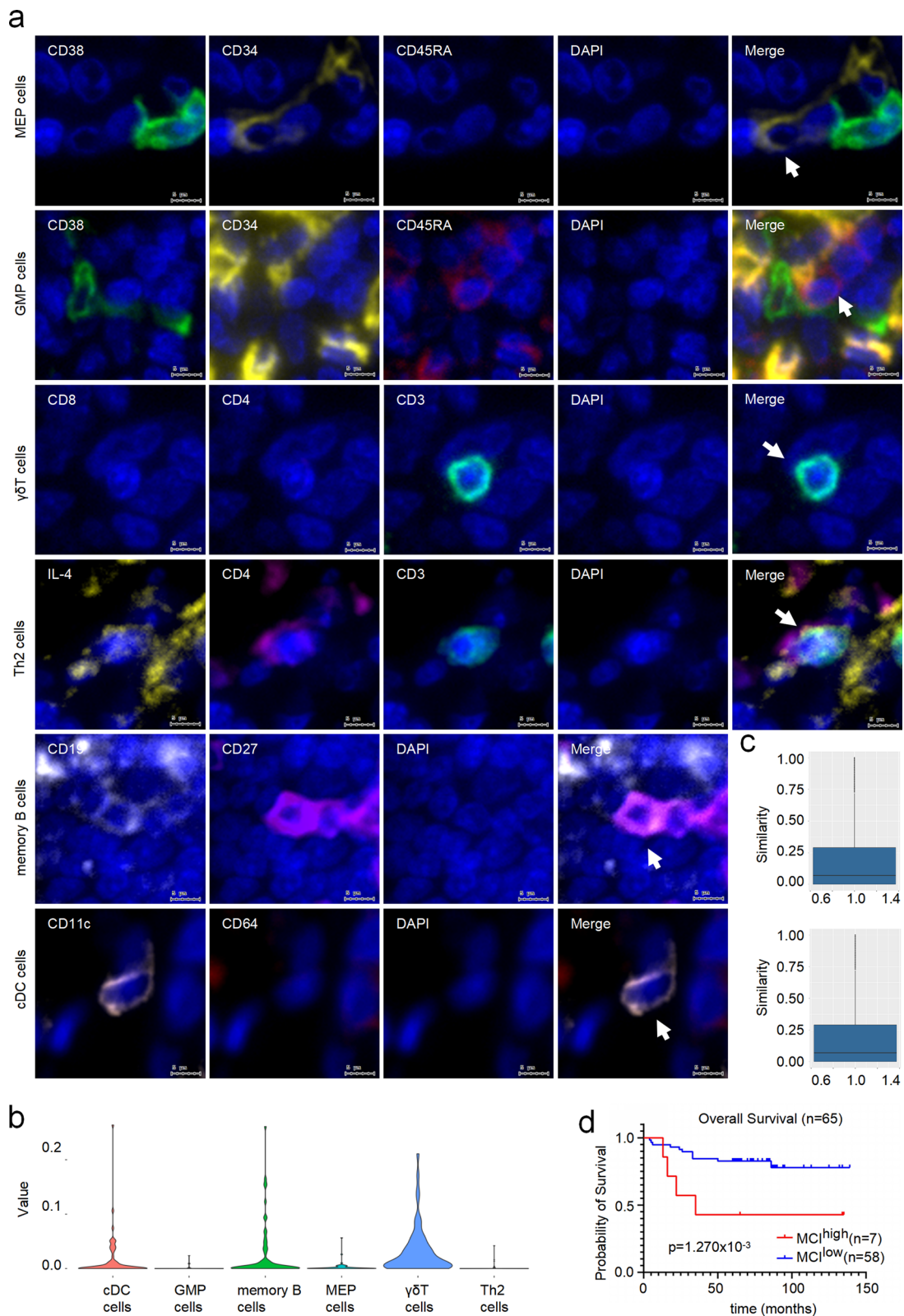
Fig. 4 (See legend on previous page.)

Yang *et al. Journal of Translational Medicine*   (2025) 23:61

Page 12 of 24

and 65 patients with TNBC were divided into MCI^{high} and MCI^{low} group. Contingency table analysis revealed that MCI^{high} status was associated with the high T stage, high N stage, and high AJCC stage in the TNBC patients (Table S4). Univariate regression analysis revealed that MCI^{high} was a risk factor for short OS in the TNBC patients (Table S5). Further multivariate Cox regression analysis revealed that MCI^{high} was an independent predictor of short OS in the TNBC patients [HR (95% CI) = 7.340 (1.787-30.144), P = 0.006] (Table S5). KM analysis revealed that MCI was significantly correlated with OS in the TNBC patients and that the TNBC patients with an MCI^{high} status had a poor prognosis (P = 1.270×10^{-3}, Fig. 4d).

The MCI combined with the spatial distribution characteristics of the six types of MCs can more accurately predicts the prognosis of the TNBC patients

In addition to relative abundance, it is important to fully analyze the spatial distribution characteristics of the six types of MCs associated with MCI. Therefore, we further analyzed the distribution of these cells in the TNBC tissues in the *mIF* cohort (Fig. 5a–d). First, the phase relationship between these cells and the special structure of the TNBC tissues was observed. The six types of MCs were not distributed within or around necrotic areas (Fig. 5e, row 1) and fat (Fig. 5e, row 4; Figure S5a, b, row 4) tissues. Many memory B cells were observed along the mammary duct wall (Fig. 5e, row 2; Figure S5a, row 3), and a small number of GMPs, MEPs, and γδT cells were found around these mammary ducts (Fig. 5e, row 2; Figure S5a, row 3). GMPs, MEPs, memory B cells, and γδT cells were observed around some blood vessels (Fig. 5e, row 3), but there were also some blood vessels without these cells (Figure S5a, b, row 1 and 2). Small numbers of MEPs, memory B cells, and Th2 cells were found in the breast lobules (Fig. 5e, row 5).

By drawing the region of interest (ROI) of the TLS and the adjacent tumor focus via hematoxylin–eosin (HE) staining (Fig. 6a, b), 53 features, including the cell number, cell ratio, cell distance, area, and TLS, as well as other related spatial distribution features, were detected in the *mIF* cohort (Fig. 6c, Table S6). The distance from the MC in the TLSs to the tumor focus was calculated (Fig. 6d). Combined with the MCI and on the basis of the above characteristics with patient age and AJCC stage, the LASSO-Cox regression model revealed that 21 prognostic factors, including the cell count, cell ratio, cell-to-TLS distance, and TLS area, were significantly associated with the prognosis of the TNBC patients combined with MCI (Fig. 6e, f). The MCI-e1 model was constructed as follows (see Table S6 for variable information):

MCI-e1 = n0 of A1 × (− 6.637×10^{-5}) + n1 × (− 7.520×10^{-2}) + n0 of A2 × (− 7.241×10^{-5}) + n4 × (6.833×10^{-3}) + n6 × (5.339×10^{-3}) + R4 × (− 1.762×10^{1}) + R5 × (− 7.370) + R6 × (− 5.452×10^{1}) + R2 × (1.755×10^{1}) + MCI × (3.451×10^{1}) + Ax2 × (− 7.741×10^{-2}) + Ax3 × (3.087×10^{-2}) + Ax4 × (4.618×10^{-2}) + Ay5 × (− 3.591×10^{-2}) + Ay6 × (− 1.200×10^{-2}) + N0 × (− 9.335×10^{-1}) + r0 × (9.501×10^{1}) + r3 × (1.090×10^{2}) + r6 × (− 1.994×10^{-2}) + age × (4.510×10^{-2}) + AJCC × 1.910.

KM analysis revealed that the TNBC patients with MCI-e1^{high} tumors had a poor prognosis (P < 1.000×10^{-4}, Fig. 6g). The AUC of the MCI-e1 reached 0.908, indicating that the MCI-e1 model performed better than the MCI model (Fig. 6h).

Furthermore, since the MCI model is calculated based on the basis of the six MC type ratios, we deleted MCI features, analyzed the remaining 52 features, and screened 7 features for MCI-e2 model construction (Figure S6a). Similarly, MCI-e2 was significantly associated with the prognosis of the TNBC patients (P < 1.000×10^{-4}, Figure S6b). Patients with MCI-e2^{high} had a poor prognosis, and the AUC of the model reached 0.934 (Figure S6e). The MCI-e2 model was calculated as follows (see Table S6 for variable information):

MCI-e2 = n0 of A1 × (− 3.449×10^{-7}) + n1 × (− 5.721×10^{-2}) + n2 × (− 1.898×10^{-1}) + n3 × (4.231×10^{-2}) + n0

(See figure on next page.)

Fig. 5 Spatial distribution of MCs in the TNBC tissues visualized in the *mIF* cohort. **a–d** Panoramic image of the tissue microarray chip after mIF staining. Representative images; the diameter of the tissue point = 1.5 mm. The expression of six markers in the TNBC tissues. CD38, green; CD34, yellow; CD45RA, red; CD27, purple; CD19, white; and DAPI, blue (**a**). Distributions of GMPs (CD34$^+$CD38$^+$CD45RA$^+$, red), MEPs (CD34$^+$CD38$^+$CD45RA$^-$, orange), and memory B cells (CD19$^+$CD27$^+$, green) in the TNBC tissues (**b**). The expression of seven markers in the TNBC tissues. CD3, green; IL4, yellow; CD64, red; CD11c, pink; CD4, purple; CD8, white; and DAPI, blue (**c**). Distributions of γδT (CD3$^+$CD4$^-$CD8$^-$, yellow), Th2 cells (CD3$^+$CD4$^+$IL4$^+$, pink), and cDCs (CD11C$^+$CD64$^-$, cyan) in the TNBC tissues (**d**). **e**, Spatial relationships between GMPs, MEPs, memory B cells, and the special structure of the TNBC tissues. Left column, representative images of typical structures from HE staining. Middle column, distribution of GMPs, MEPs, and memory B cells in the TNBC tissues; representative images of cell annotations derived from the *mIF* cohort. Right column, representative images of the six-marker panel and merged mIF staining of the TNBC tissues. **f**, Spatial relationships between γδT cells, Th2 cells and cDCs and the special structure of the TNBC tissues. Left column, representative images of typical structures from HE staining. Middle column, distributions of γδT cells, Th2 cells, and cDCs in the TNBC tissues; representative images of cell annotations derived from the mIF cohort. Right column, representative images of the seven-marker panel and merged mIF staining of the TNBC tissues
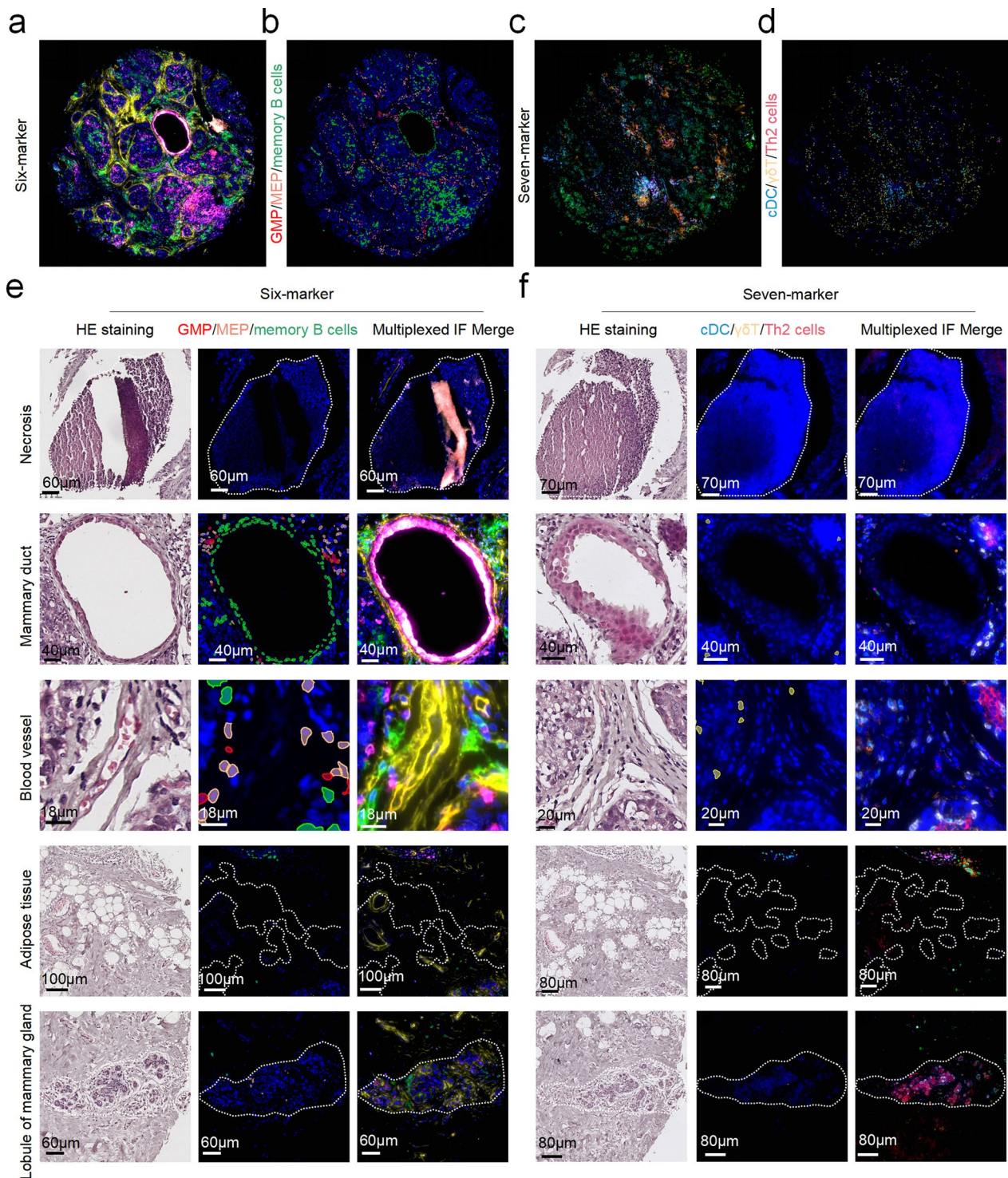
Fig. 5 (See legend on previous page.)

of $A2 \times (-\ 1.392 \times 10^{-4}) + n4 \times (4.944 \times 10^{-3}) + n5 \times (2.927 \times 10^{-1}) + n6 \times (5.635 \times 10^{-2}) + R4 \times (-4.320 \times 10^{1}) + R5 \times (-\ 8.377 \times 10^{2}) + R6 \times (-\ 7.437 \times 10^{2}) + R2 \times (2.022 \times 10^{3}) + R3 \times (-\ 8.102 \times 10^{2}) + Ax1 \times (-\ 1.415 \times 10^{-1}) + Ax2 \times$

$(-\ 5.427 \times 10^{-1}) + Ax3 \times (2.841 \times 10^{-1}) + Ax4 \times (1.585 \times 10^{-1}) + Ax6 \times (3.168 \times 10^{-2}) + N2ROI1 \times (-\ 2.989) + A$

a $\times (-4.786 \times 10^{-5}) + $ r0 of A1 $\times (7.760 \times 10^{1}) + $ r3 $\times (5.447 \times 10^{2}) + $ r4 $\times (5.959 \times 10^{2}) + $ RA2 $\times (-2.408) + $ RA5 $\times (-2.186 \times 10^{2}) + $ age $\times (6.103 \times 10^{-2}) + $ AJCC $\times 2.213$.

Finally, we removed the six types of MCs ratios from the *mIF* cohort and retained the MCI features. A total of 47 features were analyzed, and 13 features were screened for the MCI-e3 model construction (Figure S6c). Similarly, we found that MCI-e3 was also significantly associated with the prognosis of the TNBC patients ($P < 1.000 \times 10^{-4}$, Figure S6d). The prognosis of the patients with an MCI-e3^{high} status was poor, and the AUC of the model reached 0.920 (Figure S6f). The MCI-e3 model was calculated as follows (see Table S6 for variable information):

MCI-e3 = n0 of A1 $\times (-1.144 \times 10^{-4}) + $ n1 $\times (-3.438 \times 10^{-1}) + $ n3 $\times (6.917 \times 10^{-3}) + $ n0 of A2 $\times (-7.825 \times 10^{-5}) + $ n4 $\times (1.070 \times 10^{-2}) + $ n6 $\times (3.651 \times 10^{-3}) + $ MCI $\times (7.116 \times 10^{1}) + $ Ax1 $\times (-4.411 \times 10^{-2}) + $ Ax3 $\times (5.279 \times 10^{-2}) + $ N2ROI1 $\times (-2.574) + $ Aa $\times (-7.561 \times 10^{-6}) + $ r0 of A1 $\times (1.044 \times 10^{2}) + $ r3 $\times (1.419 \times 10^{2}) + $ r4 $\times (9.318 \times 10^{2}) + $ RA4 $\times 1.285 + $ RA5 $\times (-1.125 \times 10^{1}) + $ RA6 $\times (-9.860) + $ age $\times (5.501 \times 10^{-2}) + $ AJCC $\times 2.078$.

Regardless of whether the MCI-e1, MCI-e2, or MCI-e3 model was used, contingency table analysis revealed that an MCI-e^{high} status was associated with a high T stage, high N stage, and high AJCC stage in the TNBC patients (Table S4). Univariate regression analysis indicated that an MCI-e^{high} status might be a risk factor for short OS in the TNBC patients (Table S5). Further multivariate Cox regression analysis revealed that MCI-e^{high} was an independent predictor of short OS in the TNBC patients [MCI-e1: HR (95% CI) = 128.032 (5.445–3010.264), $P = 0.003$; MCI-e2: HR (95% CI) = 845.899 (11.069–64644.870), $P = 0.002$; MCI-e3: HR (95% CI) = 27.586 (4.222–180.229), $P = 0.001$] (Table S5).

We defined the TNBC patients who died in the MCI^{high}/MCI-e^{high} group as true positive and the TNBC patients who died in the MCI^{low}/MCI-e^{low} group as false negative. We also defined the TNBC patients who survived in the MCI^{high}/MCI-e^{high} group as false positive and the TNBC patients who survived in the MCI^{low}/MCI-e^{low} group as true positive. After calculation, we found MCI in the mIF cohort: positive predictive value = 4/ (4+3) $\times 100\% = 57.14\%$, negative predictive value = 46/ (46+10) $\times 100\% = 82.14\%$. MCI-e1 in the *mIF* cohort: positive predictive value = 12/(12+5) $\times 100\% = 70.59\%$, negative predictive value = 44/(44+2) $\times 100\% = 95.65\%$.

These results indicate that the MCI combined with the spatial distribution characteristics of the six types of MCs, which is called MCI-e, can more accurately predict the prognosis of the TNBC patients.

The insulin signaling pathway was significantly activated in tumor cells from the MCI^{high} TNBC patients

The TME ultimately plays an important role in cancer progression and recurrence by regulating the phenotype of cancer cells. Therefore, we aimed to determine which key signaling pathways were activated in the cancer cells of the TNBC patients in the MCI^{high} cohort to provide a reference for accurate targeted interventions.

First, we conducted enrichment analysis for the MCI^{high} and MCI^{low} patients in the *allTNBC, allTNBCsc,* and SRT cohorts and found that a total of 140 common KEGG pathways were enriched in the cancer cells of the TNBC patients in the MCI^{high} group (Fig. 7a). Next, network analysis based on the Bayesian algorithm was performed for the above 140 pathways, and the starting pathways of the Bayesian network were the insulin signaling pathways (Fig. 7b). After isolation of the TNBC cell gene expression profiling data of the *allTNBCsc* cohort, we found that the insulin signaling pathway was significantly activated in TNBC cells from the MCI^{high} subtype patients (Fig. 7c). These findings suggest that the high activity of the insulin signaling pathway may be the molecular feature of TNBC cells in the MCI^{high} patients. We subsequently analyzed the DEGs of 22 TNBC cell lines and the epithelial cell line HMEL in CCLE and conducted KEGG enrichment analysis. The first 50 pathways ($P < 0.05$) were selected from the enrichment pathways of the 22 TNBC cell lines. The insulin signaling pathway was enriched in eight cell lines (Table S7). The enriched pathways in these cell lines overlapped with 140 common pathways in all the *allTNBC*, scRNA-seq, and SRT cohorts. 47 pathways in the MDA-MB-231 cell line had the highest overlap with the above 140 pathways (Fig. 7d, e, Table S7). The above results indicate that the MDA-MB-231 cell line can be used as

(See figure on next page.)

Fig. 6 Construction of the MCI-e1 model and prediction of the prognosis of the TNBC patients. **a** TLSs (blue) and adjacent carcinoma nests (red) are outlined in the HE staining image; the diameter of the tissue point = 1.5 mm. **b** According to the results of (**a**), the TLSs (blue), and adjacent carcinoma nests (red) are outlined in the corresponding cell annotation image in the *mIF* cohort; the diameter of the tissue point = 1.5 mm. **c** Schematic diagram of TLS and carcinoma nest-related parameters. The meanings of each abbreviation are shown in Table S6. **d** Distribution of the distances from the six types of MCs to the tumor parenchyma and TLSs. **e** Features identified via LASSO-Cox analysis. **f** The distribution of LASSO-Cox coefficient profiles in cross-validation. **g** KM curve of the TNBC patients in the *mIF* cohort (n = 65) stratified by MCI-e1 score. **h** Time-dependent ROC curve indicating the accuracy of the MCI-e1 in predicting the OS rate
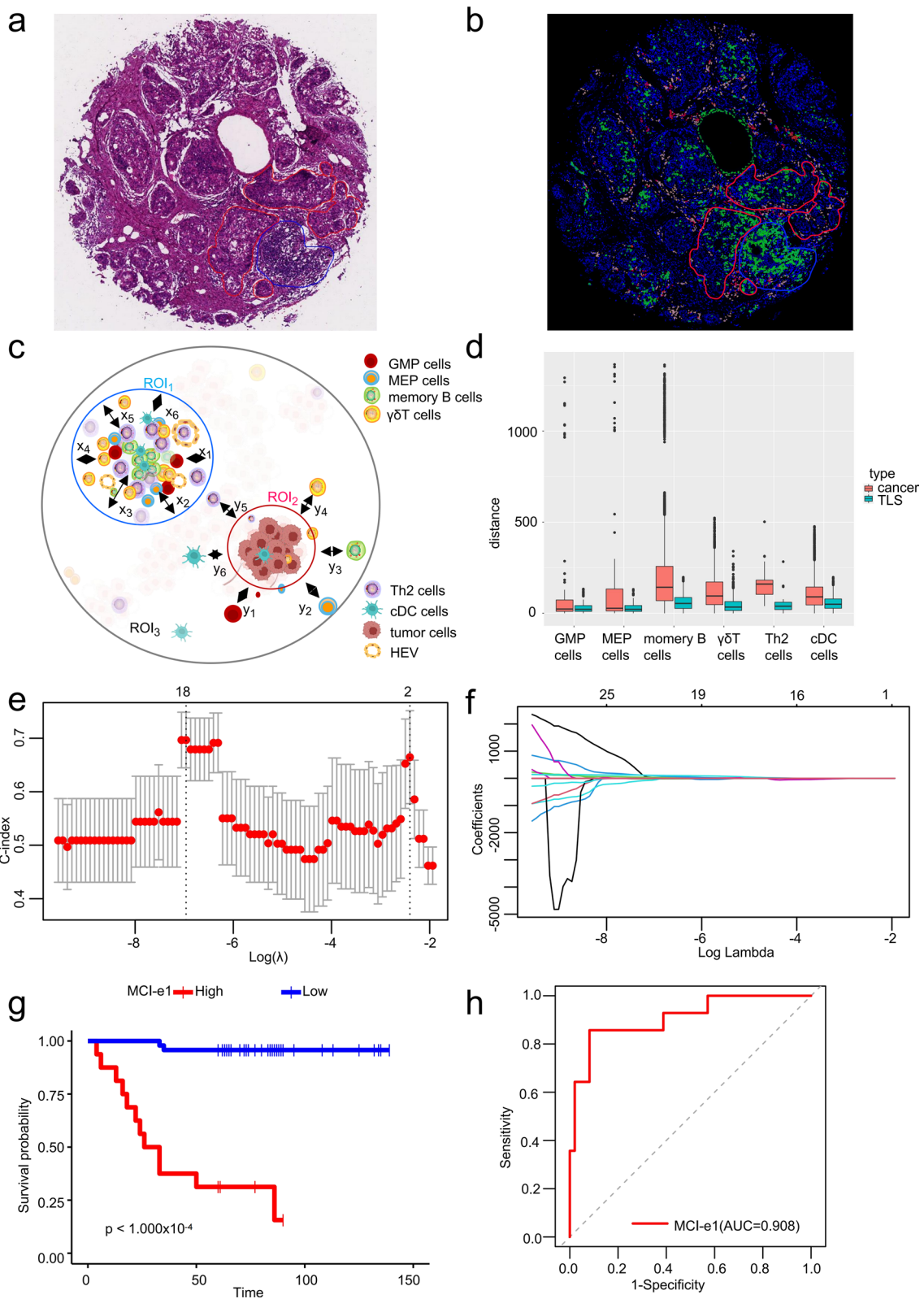
Fig. 6 (See legend on previous page.)

a tumor cell model for MCI[high] patients and that insulin signaling is a potential therapeutic target.

Inhibition of the insulin signaling pathway can prolonged the survival time of tumor-bearing mice

To evaluate the therapeutic potential of targeting the insulin signaling pathway, we next investigated whether [hydroxy (2-naphthyl) methyl] phosphonic acid (HNMPA), an inhibitor of the insulin signaling pathway, can inhibit the development of subcutaneous TNBC xenografts in a mouse model (MDA-MB-231). The mice were divided into four groups: the negative control, HNMPA, doxorubicin (DOX), and DOX + HNMPA groups (Fig. 8a; details of the dosing regimens are shown in Table S8). After 3 courses of treatment, no apparent weight loss was observed in any of the groups (Figure S7c). Compared with that in the negative control group, the growth of the xenografts in all the drug intervention groups was significantly inhibited(Figure S7a). HNMPA not only inhibited tumor growth but also increased the ability of a low dose of DOX to suppress the development of TNBC xenografts (Figure S7a). KM analysis revealed an OS advantage for the tumor-bearing mice that received continuous treatment with HNMPA alone compared with the mice that received the positive and solvent controls (Fig. 8b). The HE staining results revealed larger necrotic areas in the DOX, HNMPA, and combination groups (Fig. 8d, Figure S7b, e, f). Intriguingly, although immunodeficient NOD/SCID mice were used, abundant CD45-positive leukocytes and monocytes were present between BC tumor nests in the combination and HNMPA-treated groups (Fig. 8c–f). Specifically, obvious infiltration of immune cells, including macrophages, neutrophils, and lymphocytes, was observed in the tumor tissues of the HNMPA-treated group (Fig. 8c, Figure S7d, e). In addition, few resembling TLSs were observed in the HNMPA-treated group (Figure S7d). Similarly, the percentage of Ki67-positive cells in the DOX, HNMPA, and combination groups was significantly lower than that in the negative control group (Fig. 8g, Figure S7g), indicating that the proliferation capacity was inhibited in these three groups. In these three groups, the activation

of signaling molecules downstream of the insulin signaling pathway (p-AKT, p-ERK) was detected (Fig. 8h–j). IF analysis of insulin receptor (IR) protein expression in the MDA-MB-231 xenografts confirmed the attenuation of insulin signaling in the groups treated with the combination of DOX and HNMPA compared with the negative control group tumors (Fig. 8h–j). These functional studies demonstrated that pharmacological inhibition of the insulin signaling pathway by HNMPA attenuated the growth of TNBC xenografts and prolonged the survival time of tumor-bearing mice, which may be related to the effect of HNMPA on lymphocyte recruitment.

Discussion

Many studies have documented close relationships between tumors and the TME that dynamically shape tumor growth and development through the control of the secretion of bioactive molecules that can facilitate angiogenesis and immune evasion. Different immune cell types within the TME can also influence tumor progression, especially in patients with confirmed TNBC [38].

In this study, we constructed an infiltration profile of 64 types of MCs in TNBC, lung cancer and GBM tissues via the xCell algorithm in bulk RNA-seq data and proposed a novel prognostic model called MCI via the LASSO-Cox regression algorithm. The predictive ability of the model was rigorously validated in randomly selected validation and testing sets. Our analysis highlighted specific MCs, including GMPs, γδT cells, cDCs, and memory B cells, which exhibited protective characteristics. In contrast, MEPs and cDCs were identified as having negative implications. The six MCs collectively contribute to a robust predictive model that has emerged as a promising predictor for the clinical prognosis of the TNBC patients.

The techniques for evaluating the TME include gene expression profiling, flow cytometry, and conventional immunohistochemistry (IHC). However, these methods still have limitations [39]. Gene expression profiling can provide a comprehensive view of gene activity in tumor samples, including the gene expression patterns of immune cells and tumor cells. Bulk RNA-seq can be

---

(See figure on next page.)

Fig. 7 Functional annotation of upregulated genes in cancer cells from the MCI[high] TNBC patients. **a** Venn diagram depicting the overlapping profile of activated KEGG pathways in the tumor cells from the patients with MCI[high] in the *allTNBC, allTNBCsc,* and SRT cohorts. **b** Bayesian network analysis of the pathways. The arrow direction shows the upstream or downstream relationship between pathways, and the arrow color from blue to red represents the correlation intensity between pathways from low to high. The dots represent the total number of genes enriched in the pathway and the larger the dot is, the greater the number of enriched genes. The dot color from red to purple indicates that the *P* value of the pathway is from small to large, and red represents a small *P* value. **c** Scatter plot showing the distribution of pathway-related gene sets according to the AUCell score. **d** Venn diagram depicting the overlapping profile of activated KEGG pathways in the cancer cells of the patients with MCI[high] in the *allTNBC, allTNBCsc,* and SRT cohorts and the MDA-MB-231 cell line in the CCLE database. **e** Enrichment of 47 common pathways in MDA-MB-231 cell line. The node color is based on the *P* value, and the node radius is determined based on the number of genes
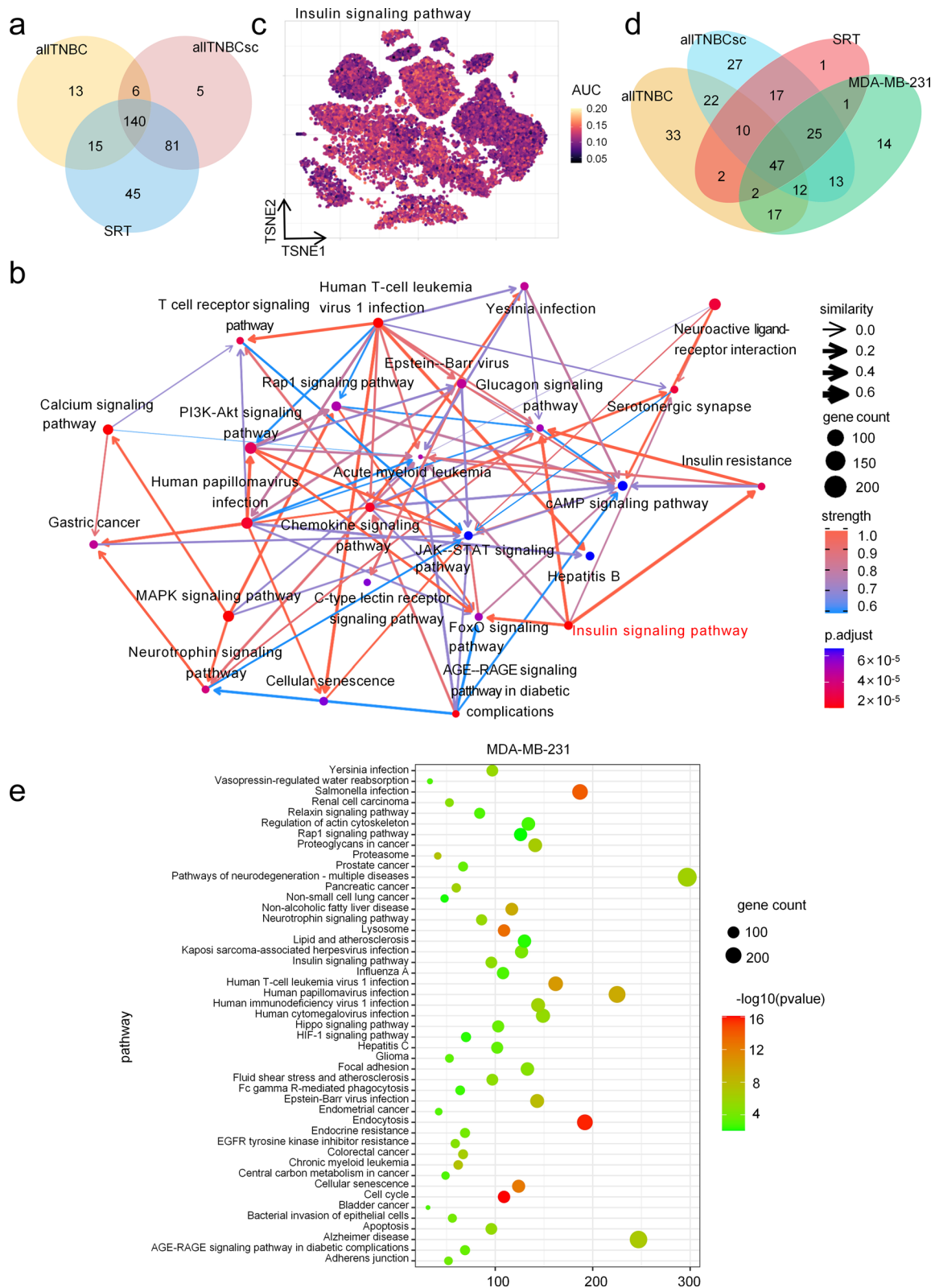
Fig. 7 (See legend on previous page.)

used to analyze the molecular spectra of tumors and stromal cells, but capturing the heterogeneity of tumor cell populations and accurately depicting the complex structure of the TME is difficult. ScRNA-seq can capture rare cell types and reveal cellular heterogeneity in the TME, which limits the study of the connections between different cells. Although transcriptome and flow cytometry analyses can be used to analyze molecules and cells in the TME, in situ spatial information cannot be obtained. While in situ information can be obtained via IHC, more than three indicators cannot be obtained, and obtaining complete descriptions of the true characteristics of highly heterogeneous cancers is difficult [40]. Notably, the interpretation of the results relies mainly on artificial qualitative and semiquantitative methods, and there is a certain degree of subjectivity. Spatial transcriptome analysis can provide single-cell-level resolution to study the cell composition, cell state, and cell interaction network in cancerous tissues. In addition, mIF staining analysis can detect multiple biomarkers in a single tissue slice, providing a unique perspective on the content, distribution, and spatial relationships of various cells in the complex TME [41]. It has high accuracy in predicting the efficacy of tumor immunotherapy and can reveal the prognosis and predictive value of immune cell subsets. In this study, the number and spatial distribution of the TME in TNBC constituent cells were precisely determined via combination analysis of multilevel expression profile data. The MCI model based on patient bulk RNA-seq data was confirmed via scRNA-seq, tissue SRT, and mIF staining assays. Moreover, the combination of the MCI and topographical characteristics of these cells was more effective at predicting the prognosis in patients with TNBC. Perhaps the most exciting of these findings is that inhibition of the insulin signaling pathway, which is significantly activated in the cancer cells of the TNBC patients with MCI^high values, could prolonged the OS of tumor-bearing mice.

Previous studies have shown that of the six types of MCs associated with in the MCI, at least three are directly related to the prognosis of the TNBC patients:

(1) γδT cells. Clinical investigations have shown that significant γδT cell infiltration is an independent prognostic factor and is associated with improved survival in the TNBC patients [17, 42, 43]. Furthermore, CAR-T cells constructed by genetically engineering γδT cells have been shown to effectively inhibit the growth of TNBC xenografts [44]; (2) Th2 cells. High infiltration of Th2 cells in BC patients is associated with tumor metastasis and poor prognosis [45, 46]. In humanized mouse models, Th2 cells accelerate BC progression and promote lung metastasis [47]. However, the exact relationship between Th2 cell infiltration and TNBC prognosis is still unclear [48]; and (3) cDCs. Accumulating evidence suggests that high infiltration of cDC1s within tumors is associated with good prognosis in various cancer patients [49–51], including the TNBC patients [52], and that infiltration of cDC1s is an independent prognostic factor associated with DFS [52]. However, the relationship between the other three MCs and the prognosis of TBNC patients is unclear: (1) GMPs. Research on the relationship between GMPs and tumors has focused mainly on leukemia [53–56]. Wu et al. reported that the increase in the number of GMPs in the circulation of the patients with tumors greatly enriches and activates myeloid immune cells and induces the rapid formation of myeloid suppressor cells, thereby promoting the progression of solid tumors [57]. However, there are currently no studies reporting the effects of GMPs on the clinicopathological characteristics, progression, treatment response, and prognosis of the TNBC patients; (2) MEPs. MEPs are progenitor cells in the bone marrow that are associated with tumor progression and poor prognosis [58–60]. Although MEPs can serve as biomarkers for predicting cancer treatment, their role and prognostic significance in TNBC are still unclear; and (3) Memory B cells. The presence of memory B cells in tumor tissue suggests the possibility of TILs [61, 62], which are positively correlated with better prognosis and response to immunotherapy in several cancer types [61, 63, 64]. In TNBC, memory B-cell infiltration significantly correlates with improved patient survival [65], suggesting that memory B-cell infiltration may be

(See figure on next page.)

Fig. 8 Inhibition of the insulin signaling pathway enhanced the immune response and prolonged the survival time of TNBC-bearing mice. **a** Schematic representation of the dosing regimen. **b** KM analysis showing the survival of the negative control (NC) (n = 6), DOX (n = 6), HNMPA (n = 7), and combination (DOX + HNMPA, n = 7) groups. The statistical significance of the differences between the four treatment groups was evaluated via the log-rank test. **c** HE staining; i, representative immune cell aggregation in HNMPA (2 mm, orange circle); ii, macrophages (50 μm, black arrow) and neutrophils (50 μm, yellow circle); iii, lymphocyte infiltration (50 μm, yellow arrow) in tumors (50 μm, red arrow); **d** HE staining, tumor necrosis (50 μm) and lymphocyte infiltration in the non-necrotic zone of tumors (50 μm, yellow arrow and green circle). **e**, **f** Expression level of CD45 (red) detected by immunofluorescence staining in the HNMPA-treated and combination-treated groups; n = 30 fields of view per group. **g** Expression level of Ki67 detected by IHC in the four groups (each group, n = 30 fields of view). **h–j** Activation of factors downstream of the insulin signaling pathway (2 μm). p-AKT (red), p-ERK (green), every group, n = 30 fields of view. The data are presented as the means ± s.t.d. Compared with those of the NC group, the statistical significance was determined via one-way ANOVA followed by Dunnett's T3 multiple comparison test
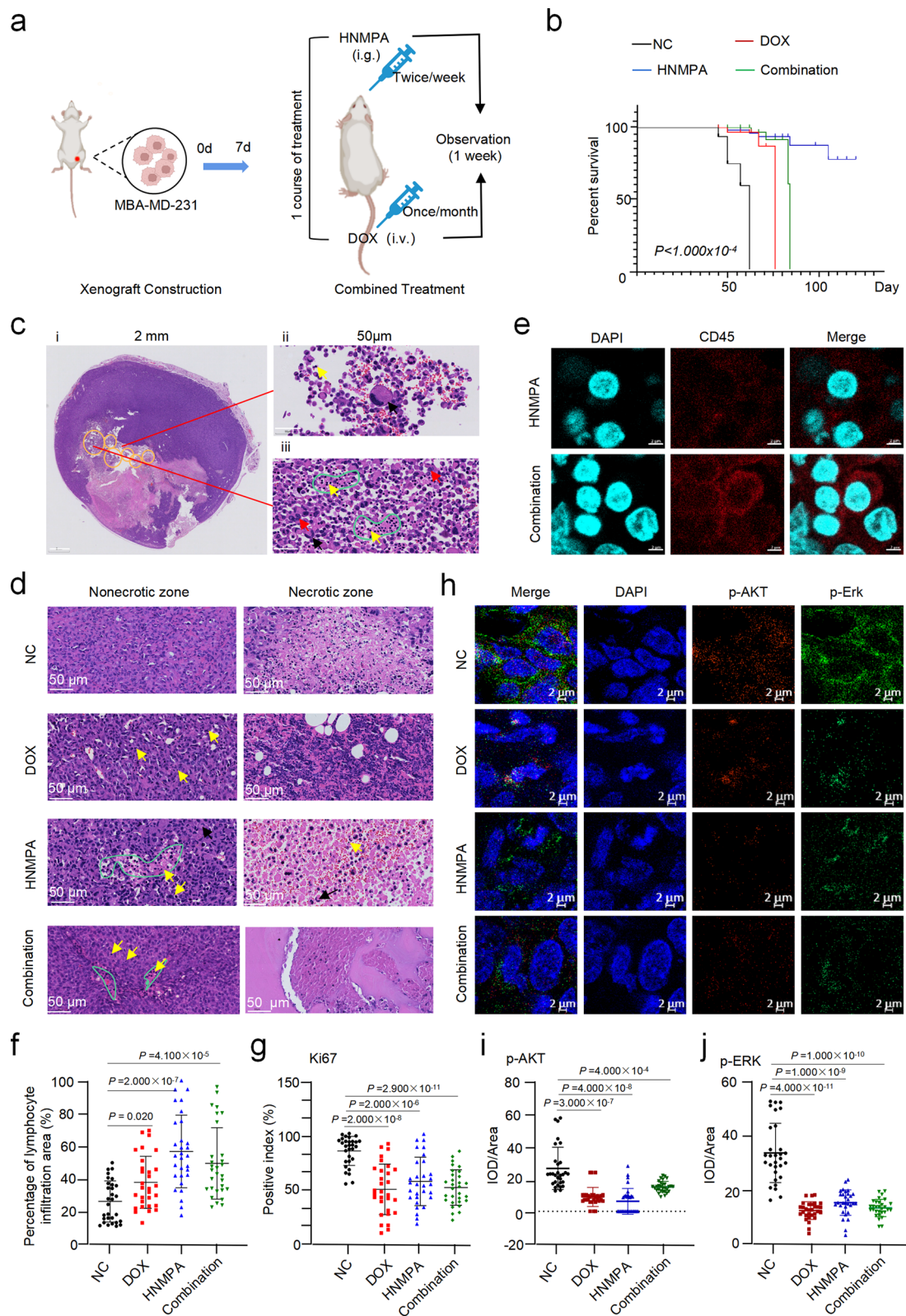
Fig. 8 (See legend on previous page.)

a potential biomarker for predicting treatment effectiveness in the TNBC patients. Compared with examining individual cells separately, our study can comprehensively evaluated the TME by integrating information from multiple cell types, thereby improving the accuracy of prognosis prediction.

The composition of the TME varies depending on the tumor type [66]. There are large differences in the type, quantity, and function of MCs infiltrating different tumors [67–69]. There are also reports from various research groups on the connection between these cells and the prognosis of the TNBC patients. According to our study, we can conclude that (1) high abundance of MCs, such as MSCs, iDCs, HSCs and CLPs, does not necessarily affect the prognosis of the TNBC patients; (2) However, the presence of multiple immune cells in the microenvironment with low abundance, such as: memory B cells, and γδT cells, significantly influences the prognosis of the TNBC patients; and (3) Previous studies on the TME have focused mainly on immune cells. Our study also confirmed that, in addition to immune cells, some stem/progenitor cells in the TME (MEPs and GMPs) have a significant correlation with the prognosis of the TNBC patients and need to be considered in future studies.

Recent results have shown that the spatial distribution of cancer cells and immune cells is a crucial predictor of the effectiveness of immunotherapy [70, 71] and that the number of cells combined with the topographical characteristics of the cells in the TME are used as prognostic predictors in various cancer types has been discussed [72]. mIF staining allows us to examine the complex cell distribution in the TME in TNBC [73]. The generation of multiple color signals on the same slide can reveal the spatial relationships between tumor cells and other cells in the TME. In our study, we built a prediction model called MCI-e to further investigate the impact of the spatial distribution of cells in the TME on the clinical prognosis of the TNBC patients. This study helps elucidate the biology of TNBC and improves the response to therapeutic regimens.

Increasing evidence suggests that abnormally increased expression of insulin and IGFs exacerbates breast tumorigenesis and promotes more aggressive phenotypes of TNBC [74–76]. In addition, Beate C Litzenburger et al. reported that insulin was highly expressed in human TNBC tumor tissue and that TNBC cells, which need additional insulin, were sensitive to BMS-754807 as an inhibitor of the IGF-IR/insulin receptor (InsR) [77]. BMS-754807 not only inhibits the proliferation of human TNBC cells but can also be used in combination with docetaxel to eliminate TNBC in PDX-TNBC models [77]. Our results consistently revealed that the insulin signaling pathway was significantly activated in the tumor cells of the TNBC patients with MCI^{high} values and that inhibition of the insulin signaling pathway effectively delayed the development of TNBC tumors in vivo. Furthermore, we found that significant lymphocyte infiltration was induced by HNMPA, which enhanced DOX-induced lymphocyte recruitment in areas around TNBC tumor nests. According to published studies, in TNBC, increased TILs in and/or around the tumor may indicate a positive response to chemotherapy and improved clinical outcome [78–82], and there has also been an increase in the number of the TLSs is associated with a favorable prognosis [83]. These results suggest that inhibition of the insulin signaling pathway could be a good adjuvant therapy for patients receiving TIL therapy. Furthermore, this study provides strong evidence that this pathway is an important potential therapeutic target for the TNBC patients with MCI^{high} values.

Conclusions

Overall, our results demonstrated that the infiltration index of MCs derived from multilevel expression profiling data can be used to predict the prognosis of TNBC, lung cancer, and GBM patients. Moreover, therapeutic strategies targeting the insulin pathway deserve further consideration and evaluation in patients with TNBC.

Abbreviations

MCs	Microenvironment cells
TNBC	Triple-negative breast cancer
bulk RNA-seq	Bulk RNA sequencing
MCI	MC index
LASSO-Cox	East absolute shrinkage and selection operator Cox
scRNA-seq	Single-cell RNA sequencing
SRT	Spatially resolved transcriptomics
mIF	Multiplex immunofluorescence
MCI-e	MCI-enhanced
ER	Estrogen receptor
PR	Progesterone receptor
Her-2	Human epidermal growth factor receptor 2
TME	Tumor microenvironment
TILs	Tumor-infiltrating lymphocytes
GBM	Glioblastoma
HSC	Hematopoietic stem
MSC	Mesenchymal stem
CLP	Common lymphoid progenitor
GMPs	Granulocyte–macrophage progenitor cells
MEPs	Megakaryocyte-erythroid progenitor cells
γδT	Gamma delta T
Th2	Type 2 T helper
cDCs	Conventional dendritic cells
IM	Immunomodulatory
M	Mesenchymal
MSL	Mesenchymal stem-like
LAR	Luminal androgen receptor
MES	Mesenchymal
BLIS	Basal-like immunosuppressed
BLIA	Basal-like immune-activated
tSNE	T-Distributed stochastic neighbor embedding
ROI	Region of interest
TLS	Tertiary lymph structure
HE	Hematoxylin–eosin

HMEL	Epithelial cell line
CCLE	Cancer Cell Line Encyclopedia
DEGs	Differentially expressed genes
HNMPA	Hydroxy(2-naphthyl) methyl phosphonic acid
DOX	Doxorubicin
BC	Breast cancer
IHC	Immunohistochemistry
DFS	Disease-free survival
Ter-cells	Erythroblast-like cells
EDMCs	Erythroid-differentiated myeloid cells
ECM	Extracellular matrix
IGF	Insulin-like growth factor
T2D	Type 2 diabetes
InsR	IGF-IR/insulin receptor
GEO	Gene Expression Omnibus
OS	Overall survival
UCSC	University of California Santa Cruz
PCA	Principal component analysis
KEGG	Kyoto Encyclopedia of Genes and Genomes
TMAs	Issue microarrays
DAPI	4′,6-Diamidino-2-phenylindole
HRs	Hazard ratios
CIs	Confidence intervals
min	Minutes
s	Seconds

Supplementary Information

The online version contains supplementary material available at https://doi.org/10.1186/s12967-024-05950-w.

Additional file 1: Figure S1–S7. **Figure S1.** Evaluation of the MCI prognostic model in the TNBC patients. **Figure S2.** Relative abundance of 64 types of MCs in TNBC. **Figure S3.** Evaluation of the MCI prognostic model in non-TNBC, lung cancer, and GBM patients. **Figure S4.** Analysis of scRNA-seq samples and the spatial distribution characteristics of four TNBC SRT samples. **Figure S5.** Spatial phase relationship between the six types of MCs and special structures in the TNBC tissues. **Figure S6.** The MCI-e2 and MCI-e3 models were constructed to predict the prognosis of the TNBC patients. **Figure S7.** Inhibition of the insulin signaling pathway enhanced the immune response of TNBC-bearing mice. Refers to Figure 8.

Additional file 2: Table S1-S9. **Table S1.** Composition and weight of the MCI patients. **Table S2.** Relationship between the MCI and clinicopathological features in the *allTNBC, trainTNBC, testTNBC1,* and *testTNBC2* cohorts. **Table S3.** Univariate and multivariate analyses of different prognostic parameters in the *allTNBC, trainTNBC, testTNBC1,* and *testTNBC2* cohorts*. **Table S4.** Relationship between MCI, MCI-e1, MCI-e2 and MCI-e3 clinicopathological features in the *mIF* cohort. **Table S5.** Univariate and multivariate analyses of different prognostic parameters in the *mIF* cohort*. **Table S6.** Characteristics of cells in the TME in the TLSs and tumor parenchyma in the *mIF* cohort. **Table S7.** Overlap of the enrichment pathways in 22 TNBC cell lines with 140 pathways. **Table S8.** Dosage regimen. **Table S9.** Clinicopathological parameters of the BRC601-1 and BRC601-2 cohorts.

Author contributions
SCY designed the study. XYY and NC performed the bioinformatic analysis. JW, NC, ZZX, XJZ, QMK, and TZ contributed to the in vitro and in vivo experiments. NC assisted with mouse surgery and tissue harvesting. XYY, JW, NC, TZ, ZZX, QMK, JZ, LPH, CHL, XYW, QW, HYJ, THS, JWX, YXZ, YD, YZ, SL and JJD collected the materials and wrote the first draft of the manuscript. XYY, JW, NC, and SCY modified the manuscript and created the figures. SCY and JW provided the funding and supervised the project. SCY revised and approved the manuscript. The Authorship order for the co-first authors was determined based on mutual agreement.

Data availability
All the materials associated with this study are presented in the paper or the Supplementary Materials. The materials that support the findings of this study are available from the corresponding author upon reasonable request. Further information and requests for resources and reagents should be directed to and will be fulfilled by the corresponding author, Shi-cang Yu (yushicang@tmmu.edu.cn).

Declarations

Ethics approval and consent to participate
All animal experimental protocols were approved by the Ethics Committee for the Use of Experimental Animals of Army Medical University (AMU-WEC20227011), and all procedures were performed under governmental and institutional guidelines and regulations. The use of two TMAs derived from the TNBC patients was granted ethical approval (XYLL-2021B001), and the study was exempted from the obligation to obtain informed consent. The Declaration of Helsinki of the World Medical Association was followed when the study was conducted.

Consent for publication
Written informed consent for publication was obtained from all participants.

Competing interests
The authors declare that they have no competing interests.

Author details
[1]Department of Stem Cell and Regenerative Medicine, Southwest Cancer Center, Southwest Hospital, Third Military Medical University (Army Medical University), Chongqing 400038, China. [2]Institute of Pathology and Southwest Cancer Center, Southwest Hospital, Third Military Medical University (Army Medical University), Chongqing 400038, China. [3]International Joint Research Center for Precision Biotherapy, Ministry of Science and Technology, Chongqing 400038, China. [4]Key Laboratory of Cancer Immunopathology, Ministry of Education, Chongqing 400038, China. [5]Jin-Feng Laboratory, Chongqing 401329, China.

References
1. Yang XY, Zheng XX, Zhai XJ, Tang T, Yu SC. Spindle apparatus coiled-coil protein 1 (SPDL1) serves as a novel prognostic biomarker in triple-negative breast cancer. Proteom Clin Appl. 2024. https://doi.org/10.1002/prca.202300002.
2. Yin L, Duan JJ, Bian XW, Yu SC. Triple-negative breast cancer molecular subtyping and treatment progress. Breast Cancer Res. 2020. https://doi.org/10.1186/s13058-020-01296-5.
3. Gajewski TF, Schreiber H, Fu Y-X. Innate and adaptive immune cells in the tumor microenvironment. Nat Immunol. 2013;14(10):1014–22. https://doi.org/10.1038/ni.2703.
4. Lu Q, Kou D, Lou S, Ashrafizadeh M, Aref AR, Canadas I, et al. Nanoparticles in tumor microenvironment remodeling and cancer immunotherapy. J Hematol Oncol. 2024. https://doi.org/10.1186/s13045-024-01535-8.
5. Whiteside TL. The tumor microenvironment and its role in promoting tumor growth. Oncogene. 2008;27(45):5904–12. https://doi.org/10.1038/onc.2008.271.
6. Xu P, Xiong W, Lin Y, Fan L, Pan H, Li Y. Histone deacetylase 2 knockout suppresses immune escape of triple-negative breast cancer cells via

Yang *et al. Journal of Translational Medicine*   (2025) 23:61

Page 22 of 24

downregulating PD-L1 expression. Cell Death Dis. 2021. https://doi.org/10.1038/s41419-021-04047-2.

7. Huang R, Wang Z, Hong J, Wu J, Huang O, He J, et al. Targeting cancer-associated adipocyte-derived CXCL8 inhibits triple-negative breast cancer progression and enhances the efficacy of anti-PD-1 immunotherapy. Cell Death Dis. 2023. https://doi.org/10.1038/s41419-023-06230-z.

8. Karn T, Pusztai L, Rody A, Holtrich U, Becker S. The influence of host factors on the prognosis of breast cancer: stroma and immune cell components as cancer biomarkers. Curr Cancer Drug Targets. 2015;15(8):652–64. https://doi.org/10.2174/1568009615081501101209.

9. Yu T, Di G. Role of tumor microenvironment in triple-negative breast cancer and its prognostic significance. Chin J Cancer Res. 2017;29(3):237–52. https://doi.org/10.21147/j.issn.1000-9604.2017.03.10.

10. Nagarajan D, McArdle SEB. Immune landscape of breast cancers. Biomedicines. 2018. https://doi.org/10.3390/biomedicines6010020.

11. Denkert C, von Minckwitz G, Brase JC, Sinn BV, Gade S, Kronenwett R, et al. Tumor-infiltrating lymphocytes and response to neoadjuvant chemotherapy with or without carboplatin in human epidermal growth factor receptor 2-positive and triple-negative primary breast cancers. J Clin Oncol. 2015;33(9):983–91. https://doi.org/10.1200/JCO.2014.58.1967.

12. Denkert C, Loibl S, Noske A, Roller M, Muller BM, Komor M, et al. Tumor-associated lymphocytes as an independent predictor of response to neoadjuvant chemotherapy in breast cancer. J Clin Oncol. 2010;28(1):105–13. https://doi.org/10.1200/JCO.2009.23.7370.

13. Melichar B, Studentova H, Kalabova H, Vitaskova D, Cermakova P, Hornychova H, et al. Predictive and prognostic significance of tumor-infiltrating lymphocytes in patients with breast cancer treated with neoadjuvant systemic therapy. Anticancer Res. 2014;34(3):1115–25.

14. Ono M, Tsuda H, Shimizu C, Yamamoto S, Shibata T, Yamamoto H, et al. Tumor-infiltrating lymphocytes are correlated with response to neoadjuvant chemotherapy in triple-negative breast cancer. Breast Cancer Res Treat. 2012;132(3):793–805. https://doi.org/10.1007/s10549-011-1554-7.

15. Bense RD, Sotiriou C, Piccart-Gebhart MJ, Haanen J, van Vugt M, de Vries EGE, et al. Relevance of tumor-infiltrating immune cell composition and functionality for disease outcome in breast cancer. J Natl Cancer Inst. 2017. https://doi.org/10.1093/jnci/djw192.

16. Danenberg E, Bardwell H, Zanotelli VRT, Provenzano E, Chin SF, Rueda OM, et al. Breast tumor microenvironment structures are associated with genomic features and clinical outcome. Nat Genet. 2022;54(5):660–9. https://doi.org/10.1038/s41588-022-01041-y.

17. Zheng S, Zou Y, Xie X, Liang JY, Yang A, Yu K, et al. Development and validation of a stromal immune phenotype classifier for predicting immune activity and prognosis in triple-negative breast cancer. Int J Cancer. 2020;147(2):542–53. https://doi.org/10.1002/ijc.33009.

18. Binnewies M, Roberts EW, Kersten K, Chan V, Fearon DF, Merad M, et al. Understanding the tumor immune microenvironment (TIME) for effective therapy. Nat Med. 2018;24(5):541–50. https://doi.org/10.1038/s41591-018-0014-x.

19. Ma Z, Wang X, Lv Q, Gong Y, Xia M, Zhuang L, et al. Identification of underlying hub genes associated with hypertrophic cardiomyopathy by integrated bioinformatics analysis. Pharmgenomics Pers Med. 2021;14:823–37. https://doi.org/10.2147/PGPM.S314880.

20. Zeng T, Cui L, Huang W, Liu Y, Si C, Qian T, et al. The establishment of a prognostic scoring model based on the new tumor immune microenvironment classification in acute myeloid leukemia. BMC Med. 2021;19(1):176. https://doi.org/10.1186/s12916-021-02047-9.

21. Bao X, Shi R, Zhao T, Wang Y, Anastasov N, Rosemann M, et al. Integrated analysis of single-cell RNA-seq and bulk RNA-seq unravels tumour heterogeneity plus M2-like tumour-associated macrophage infiltration and aggressiveness in TNBC. Cancer Immunol Immunother. 2021;70(1):189–202. https://doi.org/10.1007/s00262-020-02669-7.

22. Li J, Zhang Y, Lu T, Liang R, Wu Z, Liu M, et al. Identification of diagnostic genes for both Alzheimer's disease and Metabolic syndrome by the machine learning algorithm. Front Immunol. 2022;13:1037318. https://doi.org/10.3389/fimmu.2022.1037318.

23. Jiang H, Zhang X, Wu Y, Zhang B, Wei J, Li J, et al. Bioinformatics identification and validation of biomarkers and infiltrating immune cells in endometriosis. Front Immunol. 2022;13: 944683. https://doi.org/10.3389/fimmu.2022.944683.

24. Ueda D, Yamamoto A, Takashima T, Onoda N, Noda S, Kashiwagi S, et al. Training, validation, and test of deep learning models for classification of

25. Shimazaki A, Ueda D, Choppin A, Yamamoto A, Honjo T, Shimahara Y, et al. Deep learning-based algorithm for lung cancer detection on chest radiographs using the segmentation method. Sci Rep. 2022;12(1):727. https://doi.org/10.1038/s41598-021-04667-w.

26. Aran D, Hu Z, Butte AJ. xCell: digitally portraying the tissue cellular heterogeneity landscape. Genome Biol. 2017;18(1):220. https://doi.org/10.1186/s13059-017-1349-1.

27. Tibshirani R. The lasso method for variable selection in the Cox model. Stat Med. 1997;16(4):385–95. https://doi.org/10.1002/(sici)1097-0258(19970228)16:4%3c385::aid-sim380%3e3.0.co;2-3.

28. Qiu P, Guo Q, Yao Q, Chen J, Lin J. Characterization of exosome-related gene risk model to evaluate the tumor immune microenvironment and predict prognosis in triple-negative breast cancer. Front Immunol. 2021;12: 736030. https://doi.org/10.3389/fimmu.2021.736030.

29. Sato N, Tamada Y, Yu G, Okuno Y. CBNplot: Bayesian network plots for enrichment analysis. Bioinformatics. 2022;38(10):2959–60. https://doi.org/10.1093/bioinformatics/btac175.

30. Kaneko N, Kuo HH, Boucau J, Farmer JR, Allard-Chamard H, Mahajan VS, et al. Loss of Bcl-6-expressing T follicular helper cells and germinal centers in COVID-19. Cell. 2020;183(1):143-57 e13. https://doi.org/10.1016/j.cell.2020.08.025.

31. Ning J, Ye Y, Bu D, Zhao G, Song T, Liu P, et al. Imbalance of TGF-beta1/BMP-7 pathways induced by M2-polarized macrophages promotes hepatocellular carcinoma aggressiveness. Mol Ther. 2021;29(6):2067–87. https://doi.org/10.1016/j.ymthe.2021.02.016.

32. Wang T, Zhang J, Li N, Li M, Ma S, Tan S, et al. Spatial distribution and functional analysis define the action pathway of Tim-3/Tim-3 ligands in tumor development. Mol Ther. 2022;30(3):1135–48. https://doi.org/10.1016/j.ymthe.2021.11.015.

33. Wu F, Jiang T, Chen G, Huang Y, Zhou J, Lin L, et al. Multiplexed imaging of tumor immune microenvironmental markers in locally advanced or metastatic non-small-cell lung cancer characterizes the features of response to PD-1 blockade plus chemotherapy. Cancer Commun (Lond). 2022;42(12):1331–46. https://doi.org/10.1002/cac2.12383.

34. Liu J, Zhang S, Dai W, Xie C, Li JC. A Comprehensive prognostic and immune analysis of SLC41A3 in pan-cancer. Front Oncol. 2020;10: 586414. https://doi.org/10.3389/fonc.2020.586414.

35. Lehmann BD, Bauer JA, Chen X, Sanders ME, Chakravarthy AB, Shyr Y, et al. Identification of human triple-negative breast cancer subtypes and preclinical models for selection of targeted therapies. J Clin Invest. 2011;121(7):2750–67. https://doi.org/10.1172/JCI45014.

36. Burstein MD, Tsimelzon A, Poage GM, Covington KR, Contreras A, Fuqua SA, et al. Comprehensive genomic analysis identifies novel subtypes and targets of triple-negative breast cancer. Clin Cancer Res. 2015;21(7):1688–98. https://doi.org/10.1158/1078-0432.CCR-14-0432.

37. Wu SZ, Al-Eryani G, Roden DL, Junankar S, Harvey K, Andersson A, et al. A single-cell and spatially resolved atlas of human breast cancers. Nat Genet. 2021;53(9):1334–47. https://doi.org/10.1038/s41588-021-00911-1.

38. Li P, Li J, Tong X, Xiao Z, Diao W, Zhong C, et al. Global research trends and prospects related to tumor microenvironment within triple negative breast cancer: a bibliometric analysis. Front Immunol. 2023. https://doi.org/10.3389/fimmu.2023.1261290.

39. Lu S, Stein JE, Rimm DL, Wang DW, Bell JM, Johnson DB, et al. Comparison of biomarker modalities for predicting response to PD-1/PD-L1 checkpoint blockade: a systematic review and meta-analysis. JAMA Oncol. 2019;5(8):1195–204. https://doi.org/10.1001/jamaoncol.2019.1549.

40. Eisenstein M. Cellular censuses to guide cancer care. Nature. 2019;567(7749):555–7. https://doi.org/10.1038/d41586-019-00904-5.

41. Peng H, Wu X, Liu S, He M, Xie C, Zhong R, et al. Multiplex immunofluorescence and single-cell transcriptomic profiling reveal the spatial cell interaction networks in the non-small cell lung cancer microenvironment. Clin Transl Med. 2023;13(1): e1155. https://doi.org/10.1002/ctm2.1155.

42. Boissiere-Michot F, Chabab G, Mollevi C, Guiu S, Lopez-Crapez E, Ramos J, et al. Clinicopathological correlates of gammadelta T cell infiltration in triple-negative breast cancer. Cancers (Basel). 2021. https://doi.org/10.3390/cancers13040765.

43. Craven KE, Gokmen-Polar Y, Badve SS. CIBERSORT analysis of TCGA and METABRIC identifies subgroups with better outcomes in triple

Yang *et al. Journal of Translational Medicine*   (2025) 23:61

Page 23 of 24

negative breast cancer. Sci Rep. 2021;11(1):4691. https://doi.org/10.1038/s41598-021-83913-7.

44. Ye X, Deng X, Wen J, Li Y, Zhang M, Cai Z, et al. Folate receptor-alpha targeted 7x19 CAR-gammadeltaT suppressed triple-negative breast cancer xenograft model in mice. J Oncol. 2022;2022:2112898. https://doi.org/10.1155/2022/2112898.

45. Coussens LM, Zitvogel L, Palucka AK. Neutralizing tumor-promoting chronic inflammation: a magic bullet? Science. 2013;339(6117):286–91. https://doi.org/10.1126/science.1232227.

46. Zhou Y, Tian Q, Gao H, Zhu L, Zhang Y, Zhang C, et al. Immunity and extracellular matrix characteristics of breast cancer subtypes based on identification by T helper cells profiling. Front Immunol. 2022;13: 859581. https://doi.org/10.3389/fimmu.2022.859581.

47. Aspord C, Pedroza-Gonzalez A, Gallegos M, Tindle S, Burton EC, Su D, et al. Breast cancer instructs dendritic cells to prime interleukin 13-secreting CD4+ T cells that facilitate tumor development. J Exp Med. 2007;204(5):1037–47. https://doi.org/10.1084/jem.20061120.

48. Faucheux L, Grandclaudon M, Perrot-Dockes M, Sirven P, Berger F, Hamy AS, et al. A multivariate Th17 metagene for prognostic stratification in T cell non-inflamed triple negative breast cancer. Oncoimmunology. 2019;8(9): e1624130. https://doi.org/10.1080/2162402X.2019.1624130.

49. Zhang S, Chopin M, Nutt SL. Type 1 conventional dendritic cells: ontogeny, function, and emerging roles in cancer immunotherapy. Trends Immunol. 2021;42(12):1113–27. https://doi.org/10.1016/j.it.2021.10.004.

50. Bottcher JP, Reis e Sousa C. The role of type 1 conventional dendritic cells in cancer immunity. Trends Cancer. 2018;4(11):784–92. https://doi.org/10.1016/j.trecan.2018.09.001.

51. Maier B, Leader AM, Chen ST, Tung N, Chang C, LeBerichel J, et al. A conserved dendritic-cell regulatory program limits antitumour immunity. Nature. 2020;580(7802):257–62. https://doi.org/10.1038/s41586-020-2134-y.

52. Michea P, Noel F, Zakine E, Czerwinska U, Sirven P, Abouzid O, et al. Adjustment of dendritic cells to the breast-cancer microenvironment is subset specific. Nat Immunol. 2018;19(8):885–97. https://doi.org/10.1038/s41590-018-0145-8.

53. Jamieson CH, Ailles LE, Dylla SJ, Muijtjens M, Jones C, Zehnder JL, et al. Granulocyte-macrophage progenitors as candidate leukemic stem cells in blast-crisis CML. N Engl J Med. 2004;351(7):657–67. https://doi.org/10.1056/NEJMoa040258.

54. Minami Y, Stuart SA, Ikawa T, Jiang Y, Banno A, Hunton IC, et al. BCR-ABL-transformed GMP as myeloid leukemic stem cells. Proc Natl Acad Sci USA. 2008;105(46):17967–72. https://doi.org/10.1073/pnas.0808303105.

55. Wang Y, Krivtsov AV, Sinha AU, North TE, Goessling W, Feng Z, et al. The Wnt/beta-catenin pathway is required for the development of leukemia stem cells in AML. Science. 2010;327(5973):1650–3. https://doi.org/10.1126/science.1186624.

56. Nakahara F, Sakata-Yanagimoto M, Komeno Y, Kato N, Uchida T, Haraguchi K, et al. Hes1 immortalizes committed progenitors and plays a role in blast crisis transition in chronic myelogenous leukemia. Blood. 2010;115(14):2872–81. https://doi.org/10.1182/blood-2009-05-222836.

57. Wu WC, Sun HW, Chen HT, Liang J, Yu XJ, Wu C, et al. Circulating hematopoietic stem and progenitor cells are myeloid-biased in cancer patients. Proc Natl Acad Sci USA. 2014;111(11):4221–6. https://doi.org/10.1073/pnas.1320753111.

58. Wickrema A, Crispino JD. Erythroid and megakaryocytic transformation. Oncogene. 2007;26(47):6803–15. https://doi.org/10.1038/sj.onc.1210763.

59. Cai Q, Jeannet R, Hua WK, Cook GJ, Zhang B, Qi J, et al. CBFbeta-SMMHC creates aberrant megakaryocyte-erythroid progenitors prone to leukemia initiation in mice. Blood. 2016;128(11):1503–15. https://doi.org/10.1182/blood-2016-01-693119.

60. Han Y, Liu Q, Hou J, Gu Y, Zhang Y, Chen Z, et al. Tumor-induced generation of splenic erythroblast-like ter-cells promotes tumor progression. Cell. 2018;173(3):634–48. https://doi.org/10.1016/j.cell.2018.02.061.

61. Helmink BA, Reddy SM, Gao J, Zhang S, Basar R, Thakur R, et al. B cells and tertiary lymphoid structures promote immunotherapy response. Nature. 2020;577(7791):549–55. https://doi.org/10.1038/s41586-019-1922-8.

62. Ruffin AT, Cillo AR, Tabib T, Liu A, Onkar S, Kunning SR, et al. B cell signatures and tertiary lymphoid structures contribute to outcome in head and neck squamous cell carcinoma. Nat Commun. 2021;12(1):3349. https://doi.org/10.1038/s41467-021-23355-x.

63. Horeweg N, Workel HH, Loiero D, Church DN, Vermij L, Leon-Castillo A, et al. Tertiary lymphoid structures critical for prognosis in endometrial cancer patients. Nat Commun. 2022;13(1):1373. https://doi.org/10.1038/s41467-022-29040-x.

64. Fridman WH, Meylan M, Petitprez F, Sun CM, Italiano A, Sautes-Fridman C. B cells and tertiary lymphoid structures as determinants of tumour immune contexture and clinical outcome. Nat Rev Clin Oncol. 2022;19(7):441–57. https://doi.org/10.1038/s41571-022-00619-z.

65. Hu Q, Hong Y, Qi P, Lu G, Mai X, Xu S, et al. Atlas of breast cancer infiltrated B-lymphocytes revealed by paired single-cell RNA-sequencing and antigen receptor profiling. Nat Commun. 2021;12(1):2186. https://doi.org/10.1038/s41467-021-22300-2.

66. Anderson NM, Simon MC. The tumor microenvironment. Curr Biol. 2020;30(16):R921–5. https://doi.org/10.1016/j.cub.2020.06.081.

67. Salmon H, Remark R, Gnjatic S, Merad M. Host tissue determinants of tumour immunity. Nat Rev Cancer. 2019;19(4):215–27. https://doi.org/10.1038/s41568-019-0125-9.

68. Ganss R. Tumour vessel remodelling: new opportunities in cancer treatment. Vasc Biol. 2020;2(1):R35–43. https://doi.org/10.1530/VB-19-0032.

69. Giraldo NA, Becht E, Vano Y, Petitprez F, Lacroix L, Validire P, et al. Tumor-infiltrating and peripheral blood T-cell immunophenotypes predict early relapse in localized clear cell renal cell carcinoma. Clin Cancer Res. 2017;23(15):4416–28. https://doi.org/10.1158/1078-0432.CCR-16-2848.

70. Kather JN, Suarez-Carmona M, Charoentong P, Weis CA, Hirsch D, Bankhead P, et al. Topography of cancer-associated immune cells in human solid tumors. Elife. 2018. https://doi.org/10.7554/eLife.36967.

71. Schwen LO, Andersson E, Korski K, Weiss N, Haase S, Gaire F, et al. Data-driven discovery of immune contexture biomarkers. Front Oncol. 2018;8:627. https://doi.org/10.3389/fonc.2018.00627.

72. Morihiro T, Kuroda S, Kanaya N, Kakiuchi Y, Kubota T, Aoyama K, et al. PD-L1 expression combined with microsatellite instability/CD8+ tumor infiltrating lymphocytes as a useful prognostic biomarker in gastric cancer. Sci Rep. 2019;9(1):4633. https://doi.org/10.1038/s41598-019-41177-2.

73. Yeong J, Tan T, Chow ZL, Cheng Q, Lee B, Seet A, et al. Multiplex immunohistochemistry/immunofluorescence (mIHC/IF) for PD-L1 testing in triple-negative breast cancer: a translational assay compared with conventional IHC. J Clin Pathol. 2020;73(9):557–62. https://doi.org/10.1136/jclinpath-2019-206252.

74. Goodwin PJ. Insulin in the adjuvant breast cancer setting: a novel therapeutic target for lifestyle and pharmacologic interventions? J Clin Oncol. 2008;26(6):833–4. https://doi.org/10.1200/JCO.2007.14.7132.

75. Christopoulos PF, Msaouel P, Koutsilieris M. The role of the insulin-like growth factor-1 system in breast cancer. Mol Cancer. 2015;14:43. https://doi.org/10.1186/s12943-015-0291-7.

76. Chen WJ, Tsai JH, Hsu LS, Lin CL, Hong HM, Pan MH. Quercetin blocks the aggressive phenotype of triple-negative breast cancer by inhibiting IGF1/IGF1R-mediated EMT program. J Food Drug Anal. 2021;29(1):98–112. https://doi.org/10.38212/2224-6614.3090.

77. Litzenburger BC, Creighton CJ, Tsimelzon A, Chan BT, Hilsenbeck SG, Wang T, et al. High IGF-IR activity in triple-negative breast cancer cell lines and tumorgrafts correlates with sensitivity to anti-IGF-IR therapy. Clin Cancer Res. 2011;17(8):2314–27. https://doi.org/10.1158/1078-0432.CCR-10-1903.

78. Stanton SE, Disis ML. Clinical significance of tumor-infiltrating lymphocytes in breast cancer. J Immunother Cancer. 2016;4:59. https://doi.org/10.1186/s40425-016-0165-6.

79. Wang S, Sun J, Chen K, Ma P, Lei Q, Xing S, et al. Perspectives of tumor-infiltrating lymphocyte treatment in solid tumors. BMC Med. 2021;19(1):140. https://doi.org/10.1186/s12916-021-02006-4.

80. Lim AR, Shin SW. Tumor-infiltrating lymphocyte therapy in advanced melanoma. N Engl J Med. 2023;388(9):859. https://doi.org/10.1056/NEJMc2300132.

81. Stevanovic S, Helman SR, Wunderlich JR, Langhan MM, Doran SL, Kwong MLM, et al. A phase II study of tumor-infiltrating lymphocyte therapy for human papillomavirus-associated epithelial cancers. Clin Cancer Res. 2019;25(5):1486–93. https://doi.org/10.1158/1078-0432.CCR-18-2722.

82. Federico L, McGrail DJ, Bentebibel SE, Haymaker C, Ravelli A, Forget MA, et al. Distinct tumor-infiltrating lymphocyte landscapes are associated with clinical outcomes in localized non-small-cell lung cancer. Ann Oncol. 2022;33(1):42–56. https://doi.org/10.1016/j.annonc.2021.09.021.

Yang *et al. Journal of Translational Medicine*   (2025) 23:61

Page 24 of 24

83. Paijens ST, Vledder A, de Bruyn M, Nijman HW. Tumor-infiltrating lympho-cytes in the immunotherapy era. Cell Mol Immunol. 2021;18(4):842–59. https://doi.org/10.1038/s41423-020-00565-9.

Publisher's Note